

Evaluation of a Novel Hand Held Gamma Camera for Intra-operative Single
Photon Emission Computed Tomography

A Thesis

Presented to

The faculty of the School of Engineering and Applied Science

University of Virginia

In partial fulfillment

of the requirements for the degree

Master of Science

by

Surabhi Balagopal Nair

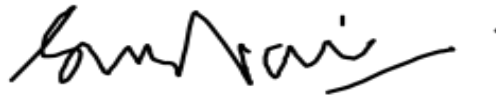
December

2016

APPROVALSHEET

The thesis
is submitted in partial fulfillment of the requirements
for the degree of

Master of Science



AUTHOR

The thesis has been read and approved by the examining committee:

Mark B. Williams

Advisor

Craig H. Meyer

Lynn T. Dengel

Accepted for the School of Engineering and Applied Science:



Craig H. Benson, Dean, School of Engineering and Applied Science

December
2016

ABSTRACT

Cancer when detected at an early stage, before it has spread, can often be treated successfully by surgery or local irradiation. However, when cancer is detected only after it has metastasized, treatments are much less successful. The lymphatic system is a primary path by which malignant cells can travel to other organs in the body. Thus determination of the presence or absence of malignant cells in lymph nodes to which a primary tumor drains is a key component of cancer staging. Sentinel lymph node biopsy (SLNB) has been developed over the past decade as a minimally invasive technique to assess regional lymph node status in patients with malignancy.

Despite its routine role in clinical management of cancer, SLNB has a higher false-negative rate (5- 10%) than is generally recognized. The current standard of care in SLNB employs a non-imaging gamma probe to locate and excise the sentinel nodes. We are exploring whether the use of a 3-D intraoperative imaging system using a hand held gamma camera could provide advantages compared to the use of the non-imaging probe. The 3-D intraoperative system has been developed through a collaborative effort involving UVa, Dilon Technologies Inc. (Newport News, Virginia), the Jefferson Lab (Newport News, VA) and SurgicEye, (München, Germany).

The system's hand held camera has a circular field of view (FOV) of diameter 60 mm and comprises a pixelated NaI(Tl) crystal array coupled to an array of silicon photomultipliers (SiPMs). In 3-D operation an optical tracking system consisting of both visual and infrared (IR) cameras tracks the location and orientation of the camera as it is moved by the surgeon. A fast iterative reconstruction algorithm uses the streamed camera data to produce and display the image of the nodes.

This thesis evaluates the 2-D and 3-D imaging performance of the hand held gamma camera system. Performance metrics include energy resolution, 2D and 3D spatial resolution, gamma ray detection sensitivity, geometric linearity, attenuation compensation, activity quantification accuracy, and the effect of scatter radiation from the radiotracer injection site.

Chapter 1 gives an overview of the current practices of sentinel lymph node biopsy and the various intra-operative surgical guidance modalities that can be used for assistance in the detection of sentinel lymph nodes. This chapter also throws light on some of the drawbacks associated with each of the modalities. Chapter 2 gives a summary of some of the contemporary small gamma cameras that have been developed and used for the detection of cancerous masses and lesions. It also introduces the declipseSPECT system with

the gamma probe and the gamma camera, which forms the crux of this thesis. Chapter 3 gives a detailed explanation of the performance evaluation experiments that were carried out using this novel gamma camera. Chapter 4 concludes this thesis, summarizing the results and comparing them with the other small gamma cameras. Chapter 5 briefly discusses the clinical studies planned with the hand held SPECT system as the next step to validate the results from this thesis.

ACKNOWLEDGMENT

I am very grateful to my adviser, Dr. Mark B. Williams for giving me the opportunity to join his lab and fund me for the duration of the course. I thank him for giving me this project, correcting me when I went the wrong way and above all, teaching me how to do research in a scientific manner. He has been a great motivator, helping me whenever I needed him. I would like to thank my committee members, Dr. Craig Meyer for helping me with the ever important statistical facet of research and Dr. Lynn Dengel for her enthusiasm and valuable surgical point of view essential for this project. I thank my fellow lab-mates, friends and family for giving me the support and encouragement, especially when things hit a roadblock. They showed me the brighter side of the picture.

TABLE OF CONTENTS

Chapter 1	1
Introduction	1
I. Current SLNB Protocol.....	4
II. Intra-Operative Surgical Guidance Modalities	7
A. Nuclear Medicine Imaging System	7
A.i) Background	7
B. Computed Tomography (CT)	12
B.i) Background	12
B.ii) Clinical Study Results.....	13
C. Magnetic Resonance Imaging (MRI)	14
C.i) Background	14
C.ii) Clinical Study Results.....	16
D. Fluorescence Molecular Imaging (FMI)	19
D.i) Background	19
D.ii) Clinical Study Results.....	20
E. Ultrasonography (US)	21

E.i) Background.....	21
E.ii) Clinical Study Results	23
III. Drawbacks	25
Chapter 2	28
NON-IMMAGING GAMMA PROBES AND Small Gamma cameras	28
I. Introduction	28
II. Contemporary Small Gamma Cameras (SGC)	30
III. DeclipseSPECT system	36
Chapter 3	45
System characterization	45
I. Introduction	45
A. Intrinsic Performance	45
B. Extrinsic performance	46
II. Performance Evaluation	46
A. Energy Resolution	46
A.i) Background	46
A.ii) Materials and methods	49

A.iii) Result	49
B. Spatial Resolution – 2D.....	50
B.i) Background	50
B.ii) Materials and Methods	52
B.iii) Result.....	53
C. Spatial Resolution 3D	55
C.i) Background	55
C.ii) Materials and Method	55
C.iii) Result.....	56
D. Sensitivity – 2D.....	57
D.i) Background	57
D.ii) Materials and Method.....	58
D.iii) Result	58
E. Sensitivity – 3D	59
E.i) Background.....	59
E.ii) Materials and Method	59
E.iii) Result.....	60

F. Depth Measurement	60
F.i) Background.....	60
F.ii) Materials and Method	61
F.iii) Result.....	62
G. Geometric Linearity	63
G.i) Background	63
G.ii) Materials and Method.....	63
G.iii) Result	66
H. Quantification of the Activity	67
H.i) Background	67
H.ii) Materials and Method.....	68
H.iii) Result	68
I. Attenuation Correction.....	70
I.i) Background	70
I.ii) Materials and Method	71
I.iii) Result.....	72
J. Effect of Injection Site	76

J.i) Background	76
J.ii) Materials and Method.....	76
J.iii) Result	78
Chapter 4	81
Conclusion.....	81
Chapter 5	84
Future Work.....	84
Reference.....	86

TABLE OF FIGURES

FIGURE 1-1: METASTASIS VIA BLOOD AND LYMPH SYSTEM	2
FIGURE 1-2: SCHEMATIC DIAGRAM OF SENTINEL LYMPH NODE BIOPSY IN THE CASE OF BREAST CANCER	6
FIGURE 1-3: FUNCTIONAL IMAGE OF BRAIN	7
FIGURE 1-4: COMPONENTS OF A GAMMA CAMERA	8
FIGURE 1-5: (LEFT) DIFFERENT TYPES OF COLLIMATORS; (RIGHT) ILLUSTRATION OF LIGHT ENERGY PRODUCTION BY SCINTILLATORS WHEN EXCITED WITH IONIZING RADIATION.....	9
FIGURE 1-6: PMT ARRAY.....	10
FIGURE 1-7: A GENERAL ELECTRIC CT SCANNER; THE INTERNAL COMPONENTS OF A CT SCANNER.....	14
FIGURE 1-8: A) RANDOM ALIGNMENT OF HYDROGEN NUCLEI IN THE ABSENCE OF AN EXTERNAL MAGNETIC FIELD. B) IN THE PRESENCE OF STRONG MAGNETIC FIELD B_1 , THE NUCLEI PRECESS IN THE DIRECTION OF THE FIELD.....	15
FIGURE 1-9: IMAGES OBTAINED USING MRI MODALITY	16
FIGURE 1-10: SIMULTANEOUS, NIR FLUORESCENT PAN-LYMPH NODE MAPPING AND SENTINEL LYMPH NODE MAPPING IN SWINE.....	21
FIGURE 1-11:(LEFT) REPRESENTATION OF AN ULTRASOUND SYSTEM;(RIGHT) INTERNAL PARTS OF A TRANSDUCER.....	22
FIGURE 1-12: (LEFT) ULTRASOUND SHOWING A SUSPICIOUS LYMPH NODE IN A WOMEN WITH BREAST CANCER; (RIGHT) ULTRASOUND OF A BENIGN MASS IN BREAST.....	24
FIGURE 2-1: A. PHOTO OF THE CAMERA AND CONTROL COMPUTER USED IN THE STUDY OF REFERENCE [44]; B. THE DETECTOR ALONE; C. CONVENTIONAL LARGE FOV ANGER CAMERA IMAGE SHOWING A SINGLE NODE (SOLID ARROW) AND THE INJECTION SITE (DASHED ARROW); D. SGC IMAGE CORRECTLY SHOWING 3 SNS (SOLID ARROWS).....	31
FIGURE 2-2: A. THE SMALL CDTE GAMMA CAMERA SYSTEM IS COMPOSED OF: DETACHABLE DETECTOR HEAD WHICH IS MOUNTED ON THE ARTICULATING ARM, CONTROL UNIT, AND POWER SUPPLY ON THE MOBILE CABINET; B. MINICAM II CAMERA HEAD (CDTE DETECTOR); C. (TOP) BOTTOM VIEW OF THE	

MEDIPROBE HEAD, C. (BOTTOM) OPEN VIEW OF THE DISASSEMBLED MEDIPROBE COMPACT GAMMA CAMERA HEAD WITHOUT THE LEAD SHIELD; D. MEDIPROBE MOUNTED ON AN ARTICULATING ARM [43].	33
FIGURE 2-3: A. THE DECLIPSESPECT SYSTEM; B. HAND HELD GAMMA CAMERA WITH THE OPTICAL TRACKING SYSTEM; C. GAMMA PROBE WITH THE OPTICAL TRACKING SYSTEM FIXED ON TOP	36
FIGURE 2-4: THE REFERENCE TARGETS THAT MAKE UP THE OPTICAL TRACKING SYSTEM	37
FIGURE 2-5: A. CAMERA SPECIFICATIONS TOP VIEW; B. CAMERA SPECIFICATIONS SIDE VIEW; C. ARRANGEMENT OF THE 80 SIPMS; D. RED SQUARE SHOWING 17 X 17 CRYSTAL REGION USED FOR IMAGING	41
FIGURE 2-6: RECONSTRUCTED IMAGE OVERLAID ON THE PHANTOM	43
FIGURE 3-1: ENERGY SPECTRUM OF ^{99m}Tc	47
FIGURE 3-2: ENERGY SPECTRUM	50
FIGURE 3-3: A. THE EXPERIMENTAL SETUP CONSISTING OF AN ANGLED CAPILLARY; B. THE IMAGE OBTAINED FROM THE ACQUISITION DISPLAYED USING IMAGE J	52
FIGURE 3-4: MEAN SPATIAL RESOLUTION 2D VS DISTANCE WITH BARS INDICATING STANDARD DEVIATION. .	54
FIGURE 3-5: EXPERIMENTAL SET UP OF CAPILLARY TUBES FOR THE CALCULATION OF 3-D SPATIAL RESOLUTION	55
FIGURE 3-6: RECONSTRUCTED IMAGE IN BOTH POSITIONS 1 AND 2 RESPECTIVELY.	56
FIGURE 3-7: EXPERIMENTAL SETUP FOR FINDING SPATIAL RESOLUTION IN THE THIRD DIMENSION	57
FIGURE 3-8: RECONSTRUCTED IMAGES OF TWO CAPILLARIES AT SEPARATION DISTANCES OF (LEFT) 25 MM, (MIDDLE) 15 MM AND (RIGHT) 10 MM	57
FIGURE 3-9: CORRECTED IMAGE OF THE 10 MM DIAMETER PETRI DISH AT 100 MM FROM THE CAMERA SURFACE	59
FIGURE 3-10: PLOT OF SENSITIVITY VS ACTIVITY	60
FIGURE 3-11: PLOT ILLUSTRATING THE DISTANCE AS MEASURED BY THE SYSTEM AND THE TRUE DISTANCE FOR 16 CASES.	62

FIGURE 3-12: A. REPRESENTATIVE EXPERIMENTAL SET UP FOR EVALUATING THE GEOMETRIC ACCURACY OF THE SYSTEM; B. REAL EXPERIMENTAL SET-UP	64
FIGURE 3-13: EXPERIMENTAL SET-UP ILLUSTRATING THE DIFFERENT CAMERA LOCATIONS AND VIEWS	65
FIGURE 3-14: PLOT OF RATIO OF TRUE % AND OBSERVED % VS OBSERVED % OF ACTIVITY	68
FIGURE 3-15: BLAND ALTMAN PLOT COMPARING THE TWO TECHNIQUES USED TO MEASURE THE RELATIVE PERCENTAGE OF THE RADIOACTIVE SOURCES.	69
FIGURE 3-16: EXPERIMENTAL SETUP	72
FIGURE 3-17: EXPERIMENTAL SETUP WITH TWO CASES TO CHECK THE EFFECT OF SCATTER ORIGINATING AT THE INJECTION SITE; (A) WITHOUT AN INJECTION SITE; (B) WITH AN INJECTION SITE OUTSIDE THE CAMERA'S FOV	77
FIGURE 3-18: EFFECTS OF SCATTER DUE TO INJECTION SITE A. ENERGY HISTOGRAM WITH NO INJECTION SITE PRESENT; B. ENERGY HISTOGRAM WITH INJECTION SITE PRESENT; C. NODE IMAGES WITH NO INJECTION SITE; D. NODE IMAGES WITH INJECTION SITE PRESENT.	78
FIGURE 3-19: EXPERIMENTAL SETUP TO CHECK THE EFFECT OF DISTANCE OF IS FROM NODES	79
FIGURE 3-20: PLOT SHOWING THE PERCENTAGE OF SCATTER OBSERVED IN THE UNIFORMITY CORRECTED IMAGE WITH INCREASING DISTANCE FROM THE NODES.....	80

CHAPTER 1

INTRODUCTION

According to the National Cancer Institute, cancer is the name given to a collection of related diseases characterized by the abnormal proliferation of cells. These have the ability to infiltrate and destroy normal body tissues, often times spreading and damaging other parts of the body [1], [2]. This process of cancerous cells breaking off and travelling to distant places in the body through the blood or the lymphatic system and forming new tumors far from the original tumors is called metastasis, as shown in Figure 1-1. When cancer is detected at an early stage, before it has spread, it can often be treated successfully by surgery or local irradiation, and the patient will be cured. However, when cancer is detected after it is known to have metastasized, treatments are much less successful[3].

The extent of lymph node metastasis is a major determinant for the staging and the prognosis of most human malignancies and often guides therapeutic decisions [4], [5]. Lymph nodes are a part of the lymphatic system which also comprises of lymph vessels and the lymphatic fluid itself. Lymph is

the clear fluid that travels through the lymphatic system and carries cells that help fight infections and other diseases.

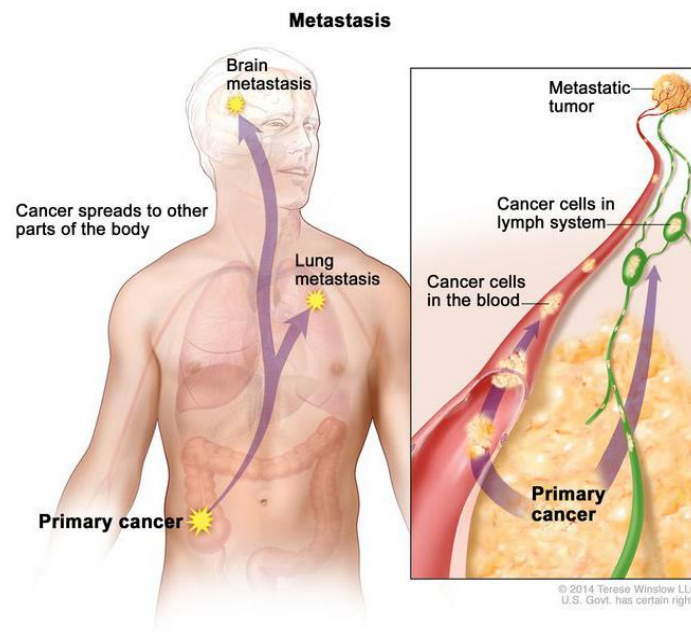


Figure 1-1: Metastasis via blood and lymph system

Reference: <http://www.cancer.gov/publications/dictionaries/cancer-terms?cdrid=46710>

Lymph nodes are small structures that work as filters of harmful substances. They contain immune cells that can help fight infection by attacking and destroying germs that are carried in through the lymph fluid [6]. Normal lymph nodes are tiny and can be hard to find, but when there's infection, inflammation, or cancer, the nodes can get larger. Those near the body's surface often get big enough to feel with your fingers, and some can even be seen. But

if there are only a few cancer cells in a lymph node, it may look and feel normal. In that case, the doctor must check for cancer by either percutaneous biopsy or removing all or part of the lymph node [6].

Sentinel Lymph Node Biopsy (SLNB) has developed over the past decade as a minimally invasive technique to assess regional lymph node status in patients with malignancy. Sentinel nodes are those located nearest the tumor(s) and thus stand sentry to the rest of the nodal basin. Hence, the cancer can spread to the nodal basin only through the sentinel nodes. Thus SLNB, in which sentinel nodes are identified and tested for the presence of malignant cells, helps in assessing the extent of metastasis by removing only a small number of nodes. This is primarily being used to diagnose breast cancer and malignant melanoma.

SLNB is elegantly simple in concept but quite often very difficult to perform accurately in individual patients [7]. Despite its routine role in clinical management of cancer, it has a higher false-negative rate than is generally recognized. In case of melanomas, an assessment of the causes of false-negative results reported that 44% of false negatives were due to failure of radiologic or surgical identification of one or more sentinel lymph nodes [8]. Hence efficient diagnostic tools are vital to ensure correct detection of cancers.

The pre-operatively obtained images are generally used to prepare the overall surgical strategy before actual surgical procedures. During surgical intervention, significant changes in tissue morphology and topology can occur. Intra-operative image guidance would provide real-time surgical guidance by providing anatomical and functional information about the operating site. This would provide in situ tissue structure and function characterization. Thus real time intra-operative imaging is essential for effective navigation throughout the surgical process [9].

I. Current SLNB Protocol

To perform a sentinel lymph node biopsy, the physician performs a lymphoscintigraphy, wherein a low-activity radioactive tracer is injected near the tumor. The injected substance, filtered sulfur colloid, is tagged with the radionuclide technetium-99m. This is taken up by the lymphatic system and travels to the sentinel nodes. The sulphur colloid is slightly acidic and causes minor stinging. A gentle massage of the injection sites spreads the sulphur colloid, relieving the pain and speeding up the lymph uptake. This injection is usually done several hours or the day before the actual biopsy[10].

Another method involves the injection of a harmless blue dye in the area near the tumor. The dye is taken up by the lymphatic system and delivered to

the sentinel nodes, staining them bright blue. The blue dye is typically injected just before the surgical procedure to remove the sentinel nodes. Typically surgeons use both the radiotracer and blue dye techniques.

The SLNB is usually performed under general anesthesia. The surgeon begins by making a small incision in the area over the lymph nodes. A small hand-held instrument called a gamma detector (refer to chapter 2 for more details) is used by the surgeon to determine where the radioactivity has accumulated and identify the sentinel nodes. The blue dye stains the sentinel nodes bright blue, allowing the surgeon to see them. The surgeon then removes these suspicious sentinel nodes. As mentioned above, sentinel nodes are the first tiers of lymph nodes to receive drainage from a malignant tumor that has metastasized. There can be multiple sentinel nodes since there can be more than one node in the vicinity of the tumor getting direct drainage from the tumor. All these nodes are removed and sent to a pathologist to examine under a microscope for signs of cancer. If cancer cells are found in the nodes by the pathologist, the lymph nodes are identified as positive lymph nodes. A negative SLNB result (sentinel lymph nodes were devoid of cancer cells) suggests that cancer has not developed the ability to spread to nearby lymph nodes or other organs. A positive SLNB result indicates that cancer is present in the sentinel lymph node and may be present

in other nearby lymph nodes (called regional lymph nodes) and, possibly, other organs. This information is then used by doctors to determine the stage of the cancer (extent of the disease within the body) and develop an appropriate treatment plan [10]. The entire procedure is described in Figure 1-2.

In some cases, sentinel node biopsy is done at the same time as surgery to remove the cancer. In other cases, sentinel node biopsy can be done before or after removal of the cancer.

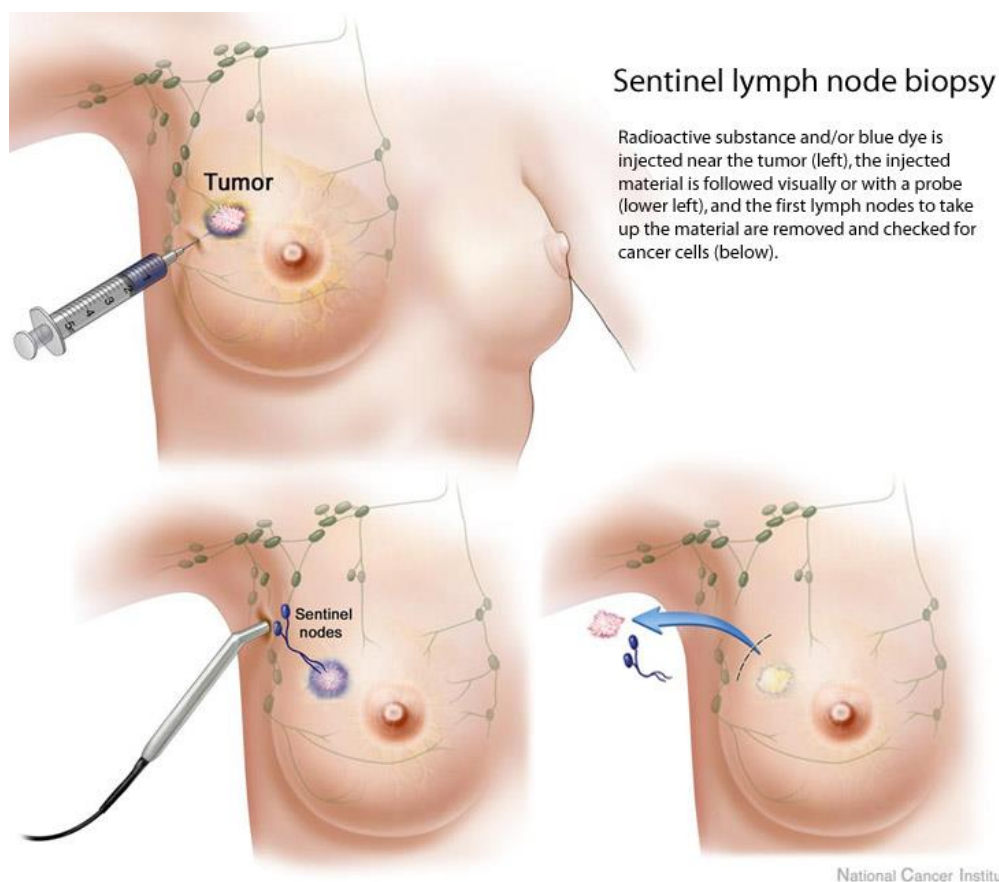


Figure 1-2: Schematic diagram of Sentinel Lymph Node Biopsy in the case of breast cancer

Reference: <http://www.cancer.gov/>

II. Intra-Operative Surgical Guidance Modalities

A. Nuclear Medicine Imaging System

A.i) Background

SLNB uses nuclear medicine imaging (lymphoscintigraphy) for pre-surgically locating the sentinel nodes.

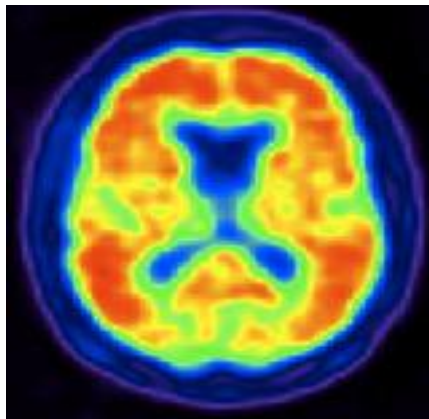


Figure 1-3: Functional image of Brain

Reference: <https://www.nibib.nih.gov/science-education/science-topics/nuclear-medicine>

The National Institute of Biomedical Imaging and Bioengineering defines nuclear medicine as a medical specialty that uses radioactive tracers (radiopharmaceuticals) to assess bodily functions and to diagnose and treat disease. Specially designed cameras allow doctors to track the path of these radioactive tracers. Single Photon Emission Computed Tomography or SPECT

and Positron Emission Tomography or PET scans are the two most common imaging modalities in nuclear medicine. Figure 1-3 shows a functional image of the brain obtained using nuclear medicine technology. In this thesis, I will be focusing on SPECT specifically [11].

The specially designed camera in the case of SPECT is called a gamma camera. The internal components that make up the camera as shown in Figure 1-4 are:

1. Collimator
2. Detector crystal
3. Photomultiplier tube array
4. Position logic circuit

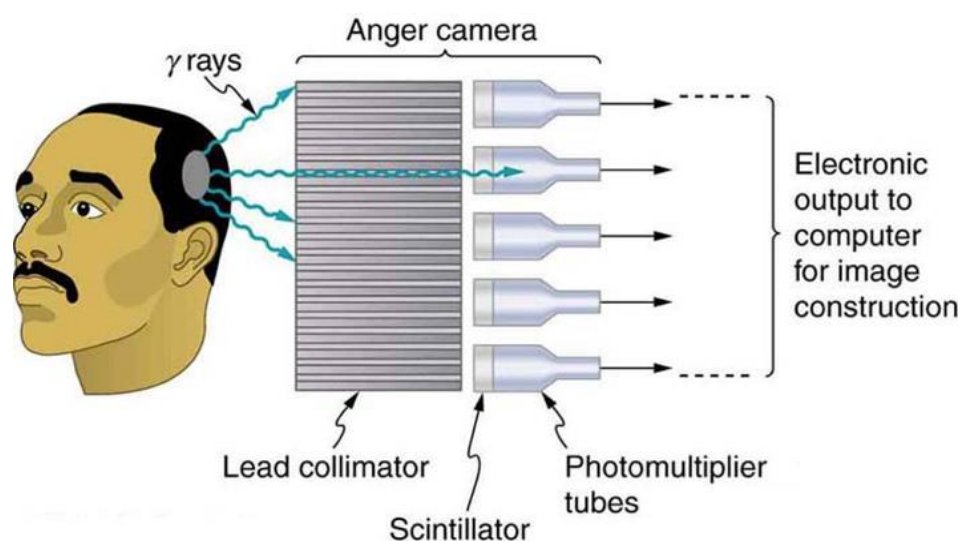


Figure 1-4: Components of a gamma camera

Reference: http://199.116.233.101/index.php/Instrumentation_SPECT

Collimators use high-attenuation materials such as lead or tungsten to permit only gamma incident in certain directions to reach the crystal. Apertures (holes) in the collimator define the allowed incidence direction. These apertures can be parallel to each other, converging or diverging providing parallel hole, magnifying (converging) or minifying (diverging) collimators respectively. Refer to Figure 1-5. The parallel hole collimator is the collimator type most often used in either 2-D or 3-D single photon imaging. A parallel hole collimator permits only those gamma rays that are incident in a direction parallel to the hole axes to pass through.

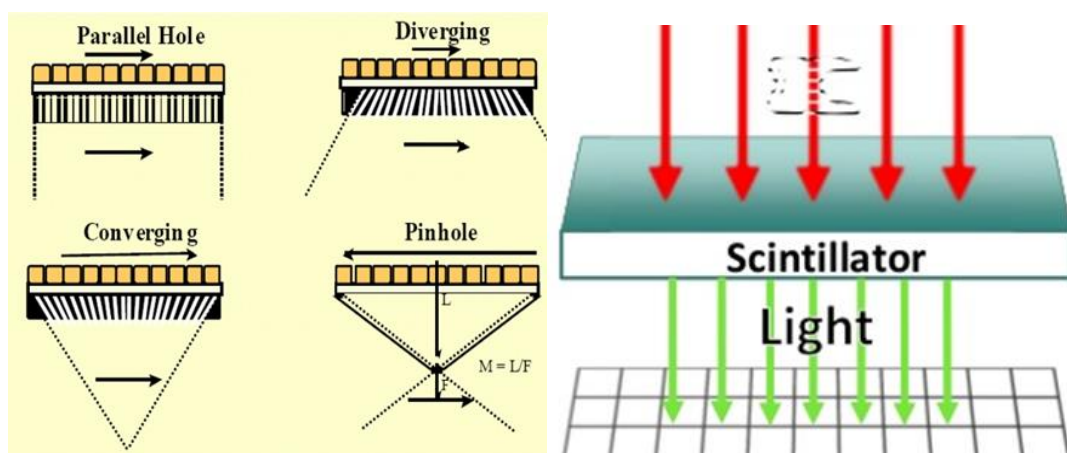


Figure 1-5: (Left) Different types of collimators; (Right) Illustration of light energy production by scintillators when excited with ionizing radiation.

Reference: <http://oftankonyv.reak.bme.hu/tikiindex.php?page=Collimators;>
<http://www.slideshare.net/bohammarlund/scintx>

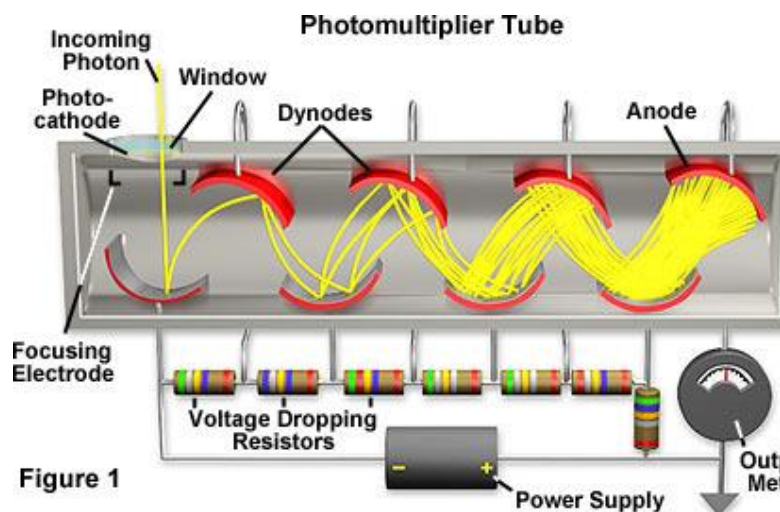


Figure 1-6: PMT array

Reference: <https://micro.magnet.fsu.edu/primer/digitalimaging/concepts/photomultipliers.html>

A scintillation crystal is coupled to a PMT, which is schematically shown in Figure 1-6. The inside of the entrance window of the evacuated glass envelope is covered with a photocathode that converts photons into electrons. The emitted electrons are focused onto the first dynode by means of an electric field created by biasing the photocathode and dynodes, as indicated by the external power supply and voltage divider in Figure 1-6. The applied voltage depends on the PMT design, and is in the range of 200–1500 V. The progressively more positive potential of each dynode causes the electrons leaving the photocathode (photoelectrons) as well as those leaving the dynodes (secondary electrons) to be accelerated towards the next dynode. If an electron of sufficient energy hits

a dynode, electrons are released by secondary emission. Typical dynode materials are BeO–Cu, Cs₃Sb and GaP:Cs, which exhibit high secondary emission properties. These electrons are then accelerated and focused onto the next dynode and secondary electrons are emitted, etc. The number of dynodes n is in the range of 8–12. The signal is obtained from the last electrode, the anode. PMT electron gains of up to 10^6 – 10^7 are obtained [12]. The size of the charge pulse arriving at the anode is proportional to the number of light photons incident on the photocathode.

In a conventional gamma camera as shown in Figure 1-4 the light photons originating from the point of gamma ray absorption in the crystal spread out from the absorption point so that light is detected by multiple PMTs. By connecting the anodes of the camera's PMTs together using Anger circuitry the centroid of the light pulse can be determined to a much greater degree of precision than the PMT spacing. The sum of the charge from all PMTs is proportional to the amount of energy deposited in the crystal by the gamma ray [13]. Clinical trial results using gamma camera is discussed below in chapter 2.

B. Computed Tomography (CT)

B.i) Background

Computed tomography (CT) as defined by the National Cancer Institute is an imaging procedure that uses special x-ray equipment to create detailed pictures, or scans, of areas inside the body [14], [15].

As described by the National Institute of Biomedical Imaging and Bioengineering, CT scanner consists a motorized x-ray source that rotates around the circular opening of a donut-shaped structure called a gantry. During a CT scan, the patient lies on a bed that slowly moves through the gantry while the x-ray tube rotates around the patient, shooting narrow beams of x-rays through the body. CT scanners use special digital x-ray detectors, which are located directly opposite the x-ray source. As the x-rays pass through and leave the patient, they are picked up by the detectors and transmitted to a computer.

After one full rotation of the x-ray source, the CT computer uses sophisticated mathematical techniques to construct a 2D image slice of the patient. The thickness of the tissue represented in each image slice usually ranges from 1-10 millimeters. When a full slice is completed, the image is stored and the motorized bed is moved forward incrementally into the gantry. The x-ray scanning process is then repeated to produce another image slice. This

process continues until the desired number of slices is collected. These Image slices can either be displayed individually or stacked together by the computer to generate a 3D image of the patient that shows the skeleton, organs, and tissues as well as any abnormalities the physician is trying to identify [15]. A CT system and its internal structure of CT are shown in Figure 1-7.

B.ii) Clinical Study Results

CT in conjunction with Single Photon Emission Tomography (SPECT) or SPECT/CT combination is a new tool which has potential application in sentinel node imaging. This dual modality provides complementary functional and anatomical information and thus is superior to planar imaging [16]. Images from each modality can be fused or used separately.

Wagner *et al.* describes the advantages of using such a combination. These include improved anatomical localization of sentinel lymph nodes and alteration in the surgical approach, identification of false positive planar findings of hot nodes and better detection rates of sentinel lymph nodes due to better spatial resolution [16]. Valdes et al and other studies also provide similar result [17].

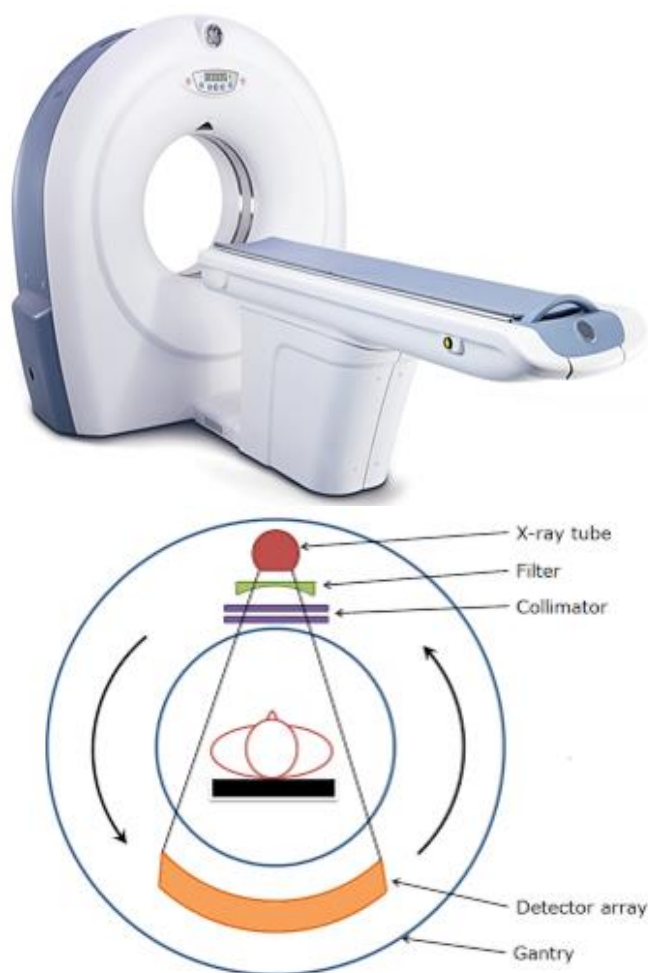


Figure 1-7: A General Electric CT Scanner; the internal components of a CT scanner

Reference: (Top) <http://www3.gehealthcare.in/en/products/categories/computed-tomography>;
(bottom) <https://sites.google.com/site/frcrphysicsnotes/ct-equipment>

C. Magnetic Resonance Imaging (MRI)

C.i) Background

MRI involves imaging the protons that are abundantly prevalent in human body. Protons are the positively charged spinning Hydrogen nucleus and thus have

a small magnetic field due to their spin and charge. Thus when a human body is placed in a large magnetic field, many of the free hydrogen nuclei align themselves with the direction of the magnetic field (Figure 1-8). The nuclei precess about the magnetic field direction like gyroscopes. This behavior is termed Larmor precession [18].

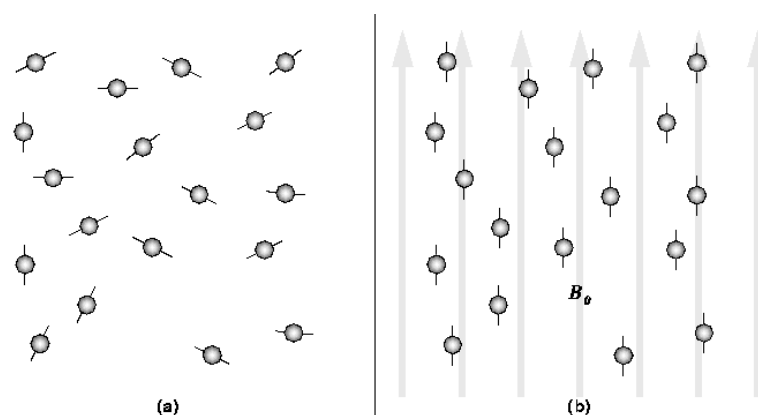


Figure 1-8: a) Random alignment of hydrogen nuclei in the absence of an external magnetic field.
b) In the presence of strong magnetic field B_1 , the nuclei precess in the direction of the field

Reference: <https://www.cs.sfu.ca/~stella/papers/blairthesis/main/node11.html>

The nuclei can be rotated using radio waves, and once these radio waves are removed, they subsequently oscillate in the magnetic field while returning to equilibrium. Simultaneously they emit a radio signal. This is detected using antennas (coils) and can be used for making detailed images of body tissues. The frequencies used is typically in the range of 40-130 MHz. Very detailed images

can be made of soft tissues such as muscle and brain (Figure 1-9). The MR signal is sensitive to a broad range of influences, such as nuclear mobility, molecular structure, flow and diffusion. MRI is consequently a very flexible technique that provides measures of both structure and function.

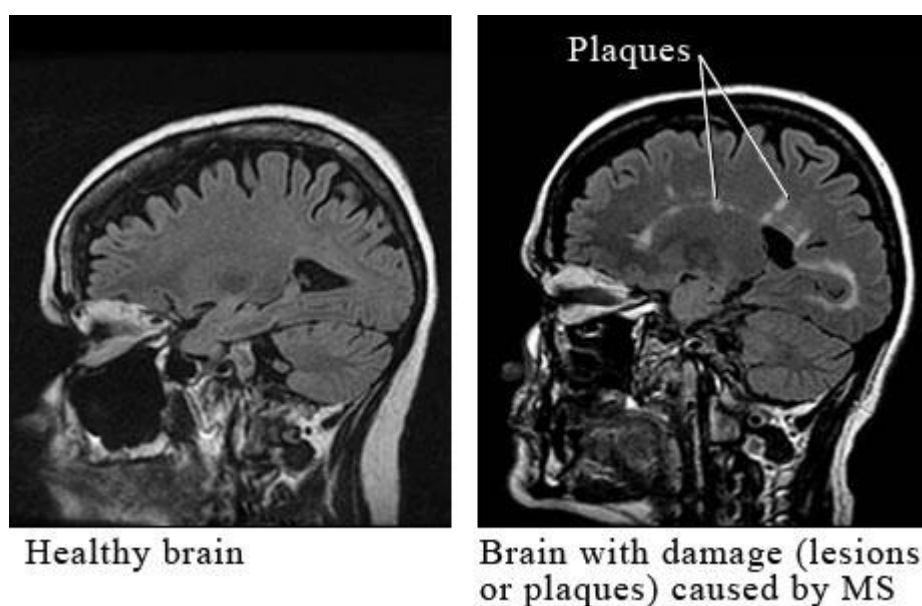


Figure 1-9: Images obtained using MRI modality

Reference: <http://www.webmd.com/multiple-sclerosis/magnetic-resonance-imaging-mri-of-multiple-sclerosis>

C.ii) Clinical Study Results

Breast MRI using gadolinium-based contrast agents is a commonly used component of breast cancer clinical care. Clinical research studies have shown contrast-enhanced MRI to have a very high sensitivity for breast lesions. Some

lesions are, even in retrospect, not detectable in mammographic x-ray or breast ultrasound images but are detectable via MRI. MRI breast imaging as a guide in interventional procedures such as interstitial laser therapy (ILT), radiofrequency ablation (RFA), high-intensity focused ultrasound (HIFU), microwave ablation therapy, and cryotherapy is also being studied [19].

Another very recent study was conducted by Li *et al.* to evaluate magnetic resonance lymphography with a gadolinium-based contrast agent (Gd-MRL) in sentinel lymph node identification in patients with breast cancer. Sixty patients (mean age: 46.2 ± 8.8 years) with stage T1- 2 breast cancer and clinically negative axillary lymph nodes participated in this study. After 0.9 ml of contrast material and 0.1 ml of mepivacaine hydrochloride 1% were mixed and injected intradermally into the upper-outer periareolar areas, axillary lymph flow was tracked and sentinel lymph nodes were identified by Gadolinium based Magnetic Resonance Lymphography (Gd-MRL).

With Gd-MRL, the lymph vessels from the injection site to the axilla were stained. The SLN was defined as the first lymph node visualized on the lymph vessel draining directly from the injection site. In some patients, more than one lymphatic vessel drained directly from the injection site. In these patients, the first visualized lymph node along each lymphatic vessel draining directly from

the injection site was considered a sentinel node. This was followed by marking the sentinel nodes using a skin marker method.

SLN biopsy and/or surgery was then performed and the efficacy of SLN identification and consequently metastasis detection of Gd-MRL were examined by the histopathologic evaluations of the resected lymph node. If the lymph nodes were positive for lymph nodes, metastasis was established. Using blue dye-guided methods as the gold standard, the sensitivity of Gd-MRL was 95.65% and the false-negative rate was 4.3% for axillary lymphatic metastasis detection [20].

The various studies conducted by different research groups indicate that MRI as a diagnostic tool for excluding axillary lymph node metastases and can potentially replacing SLNB. The diagnostic performance of some MRI protocols approaches the negative predictive value (NPV) needed to replace SLNB. However, current observations are based on studies with heterogeneous study designs and limited population [21]. Another study indicates that sentinel nodes can be detected accurately by a combination of SLNB and MRI guided lymph node sampling [22]. Thus this approach needs to be studied more before coming to a concrete conclusion.

D. Fluorescence Molecular Imaging (FMI)

D.i) Background

Fluorescence molecular imaging (FMI) is a powerful tool that can be used for precise guidance and localization of malignant tissues intraoperatively. In FMI an optical imaging system is used intraoperatively to help surgeons distinguish between normal and malignant tissues following the injection of an agent labeled with a fluorescent compound [23]. In most cases the fluorophore emits in the near infrared (NIR) and is also excited with NIR light. NIR excitation and emission permits much deeper tracer visualization compared with tracers labeled with visible fluorophores because of the superior tissue penetration of NIR light (wavelengths between ~700 nm and 1200 nm) compared to visible light. The use of NIR excitation also has the advantage of reducing tissue autofluorescence compared to that present with shorter wavelength light excitation.

Once the fluorescent agent is injected, a surgical navigation system is required to activate the NIR fluorophore by illumination with NIR light. Video rate images using a NIR-sensitive camera are provided by the system for surgical guidance, typically after fast image registration of the NIR image with a conventional visible light image. These techniques have been demonstrated to be effective for providing surgeons with precise tumor detection in real-time

during surgery. Current studies suggest that FMI technology can assist surgeons in resecting micro-cancer tissues down to the submillimeter size, thus improving patient outcome [23], [24].

D.ii) Clinical Study Results

Khullar *et al.* developed the Fluorescence-Assisted Resection and Exploration (FLARE™) system which utilizes NIR light-emitting diode (LED) excitation, instead of a potentially harmful laser. It has the advantage of being able to provide simultaneous color imaging, NIR fluorescence imaging, and color-NIR merged images, allowing the surgeon to simultaneously visualize invisible NIR fluorescence images within the context of surgical anatomy, illustrated in Figure 1-10 [25].

Troyan *et al.* discusses the successful clinical translation of a new NIR fluorescence imaging system for image-guided oncologic surgery [26]. Ngyuen *et al.* discusses the use of fluorescently labelled markers for intra-operative surgical molecular navigation to display tumors and nerves in real time. This allows more complete tumour resection while preserving important structures around the tumour [27].

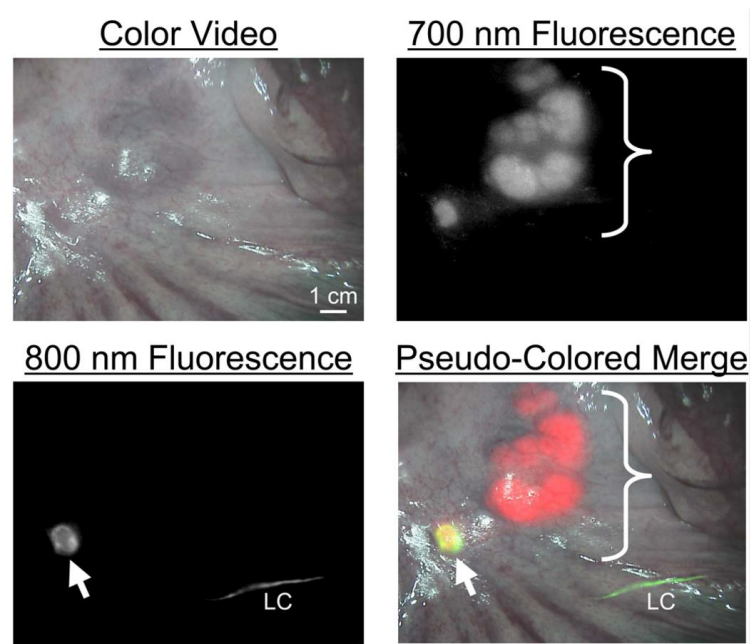


Figure 1-10: Simultaneous, NIR Fluorescent Pan-Lymph Node Mapping and Sentinel Lymph Node Mapping in Swine

E. Ultrasonography (US)

E.i) Background

Ultrasound (US) is a diagnostic imaging technique based on the propagation and reflection of ultrasound waves. The NCBI (National Centre of Biotechnology Information) defines US as the visualization of deep structures of the body by recording the reflections or echoes of ultrasonic pulses directed into the tissues. Ultrasound for imaging or diagnostic purposes employs frequencies ranging from 1.6 to 10 megahertz [28].

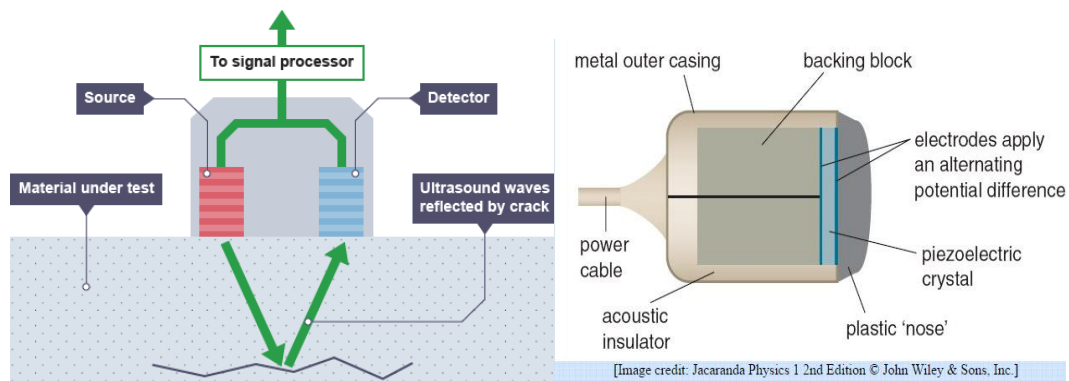


Figure 1-11:(Left) Representation of an Ultrasound system;(Right) Internal parts of a transducer

Reference:<http://www.bbc.co.uk/education/guides/zwjsgk7/revision/3>;
http://www.genesis.net.au/~ajs/projects/medical_physics/ultrasound/

The ultrasound beam originates from mechanical oscillations of numerous crystals in a transducer, which are excited by electrical pulses by way of the piezoelectric effect. The transducer converts electrical energy into mechanical energy in the form of sound waves. The ultrasound waves are emitted in short pulses that are sent from the transducer and propagate through the different tissues. A portion of the emitted pulse returns to the transducer after reflection from the tissues. The returned echoes are converted back into electrical impulses by the transducer crystals and are further processed in order to form the ultrasound image [29]. This is shown in Figure 1-11.

E.ii) Clinical Study Results

Ultrasound images of a suspicious lymph node and a benign mass in the human breast is shown in Figure 1-12. Axillary US in case of breast cancer metastasis provides with identification of the lymph nodes, assessment of even the smallest nodes, and in-depth evaluation of node morphology. In US, the images of the nodes are generally assessed for size, shape, visibility and morphology of the hilum (depression on the surface of lymph nodes through which blood vessels enter and leave the node), vascularity, and focal cortical thickening [30].

Nori *et al.* studied the preoperative diagnostic accuracy of axillary US. Two shape parameters were considered: the ratio between longitudinal diameter and transverse diameter (L/T ratio), which is ≥ 2 in normal lymph nodes, and the ratio between hilum diameter (H) and longitudinal diameter (L) of the lymph node (H/L ratio), normal lymph nodes being considered those with a hilum diameter $\geq 50\%$ of the overall longitudinal diameter (H/L ratio $\geq 50\%$).

Metastatic nodes tend to have globular morphology (L/T ratio = 1) and compression or disappearance of the hilum (H/L ratio $< 50\%$).

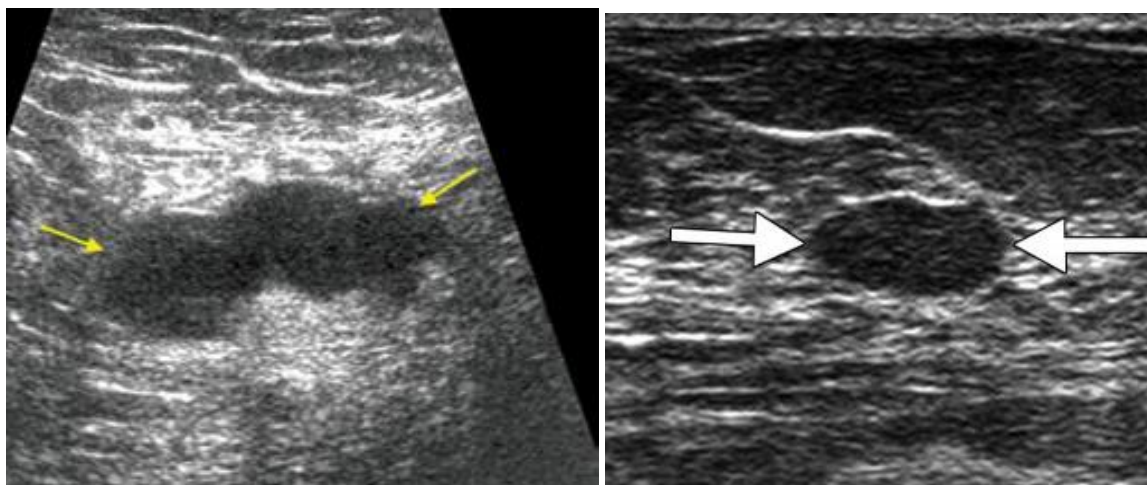


*Figure 1-12: (Left) Ultrasound showing a suspicious lymph node in a women with breast cancer;
(Right) Ultrasound of a benign mass in breast*

*Reference: <https://www2.mdanderson.org/depts/oncolog/articles/13/10-oct/10-13-1.html>;
<http://oncozine.com/profiles/blogs/annual-screening-with-breast>*

The sonographic criteria considered suspicious for malignancy included:

(1) globular morphology and/or H/L ratio less than 50%; (2) disappearance of hilum fat hyper-echogenicity (increased echo response due to fat deposits); and (3) eccentric focal thickening and denting of the cortex (outer layer of node). The final histologic results concerning lymph nodal involvement were compared with the preoperative axillary node status as assessed by US. Sensitivity and specificity of axillary US alone in the detection of metastatic nodes were 45.2% and 86.6% respectively, and positive predictive value (PPV) and negative predictive value (NPV) were 61.3% and 77.2%, respectively. Overall accuracy was 73.5% [30].

Sever *et al.* intra-dermally injected microbubbles which act as US reflectors, to identify and localize SLNs preoperatively by contrast-enhanced sonography in patients with breast cancer. The microbubble contrast agent readily enters breast lymphatic channels, passing into the draining SLN, and are clearly visualized by contrast-enhanced ultrasound. SLNs were identified successfully before surgery in 89% of patients [31].

III. Drawbacks

The standard of care used in the United States during SLNB requires the use of (99m) Tc-labeled colloid, 1% isosulfan blue dye, or both to trace the lymphatic drainage of a given neoplasm. Studies have found adverse reactions to injection of isosulfan blue dye during sentinel lymph node mapping in breast cancer [32]. Also, SLNB in women diagnosed with clinically node-positive breast cancer after neoadjuvant chemotherapy proved to have higher false-negative rate, varying from 7% to 25% [33], [34]. A meta-analysis carried out to evaluate the significance of false negative rate (FNR) of sentinel lymph node biopsy in patients with breast cancer concludes that blue dye alone method has the highest FNR. This can be significantly lowered to 5% to 10% using radiotracer along with the blue dyes to detect the sentinel nodes [35], [36]. But intraoperative external gamma probe counting requires some skill for accurate

identification of the SLN. Also, the lack of being able to visualize the pre-incision anatomical relationship between tumor, lymph vessels, and SLNs when using this combination limits the surgeon's ability to decide as to where to place the surgical incision [20].

The disadvantage with CT involves greater exposure to radiation while imaging the patients. It is difficult to identify very small sentinel lymph nodes of the order of 2-3 mm using this technique. There can be potential false positive results from lymph node calcifications as well [37]. Relative changes in lymph node position before and during surgery might make CT lymphography less effective, especially for the SLN located deep in the fatty axilla [38].

MR imaging has limited resolution and cannot reliably detect micro-metastases in lymph nodes. In Gd-MRL, the intradermal toxicity or tolerance of the Gd based contrast agent needs future investigation [20]. Current observations are based on studies with heterogeneous study designs and limited population. MRI based on diffusion weighted imaging has disadvantages of high sensitivity to motion artefacts, limited spatial resolution and more pronounced artefacts at higher field strengths [21]. Thus this approach needs to be studied more before coming to a concrete conclusion.

In case of FMI, fluorescence imaging contrast agents with better targeting properties need to be approved for clinical use by the Food and Drug Administration (FDA). The fluorescent dye indocyanine green (ICG) obtained approval and has been applied to sentinel lymph node (SLN) mapping and hepatic micro-metastases detection. However, ICG lacks precise targeting properties. ICG is not highly tumor-selective and has difficulty detecting neoplastic lesions with high sensitivity and specificity [39]. Thus, more effective contrast agents need to be designed and approved by FDA for the advancement of this modality. Another disadvantage is this modality's poor depth dependent resolution [40].

The main disadvantages of US are its poor spatial resolution, the large size of the microbubble and hence its slower rate of uptake, its limited use in the thorax, and its dependence on operator experience [41].

CHAPTER 2

NON-IMMAGING GAMMA PROBES AND SMALL GAMMA CAMERAS

I. Introduction

Radio-guided surgery using a non-imaging gamma probe is an established practice and has been widely introduced in sentinel lymph node biopsies (SLNBs). The procedure provides surgeons with enhanced capabilities for accurate identification of sentinel lymph nodes, and importantly permits during-surgery histological determination of whether or not sentinel nodes contain malignant cells. If the sentinel nodes in a given nodal basin are determined to be negative, then the probability of other positive nodes in that basin is very low and further removal of nodes can be avoided. The introduction of the SLNB procedure in breast cancer has greatly reduced the post-surgical morbidity associated with radical lymph node dissection and has been demonstrated to provide similar outcomes [42].

The non-imaging gamma probe is a well-established tool frequently used in cancer management. It measures the radiation emitted by a radionuclide and gives an audio output whose frequency increases with increasing gamma

counting rate. These are particularly used in tumor localization to detect radio-markers pre-operatively implanted in tumors and also to detect sentinel lymph nodes following injection of a radiolabeled colloidal compound designed to become trapped in the nodes.

In conventional SLNB, pre-surgical lymphoscintigraphy is performed using a large field of view (FOV) gamma camera as described in Chapter 1. Imaging takes place after the tracer is injected near the tumor, allowing sufficient time for drainage to the nearby nodes. Then either later that day or on the following morning, following pre-surgical review of the lymphoscintigraphic images, a non-imaging gamma probe is used intra-operatively to locate and excise the sentinel nodes. Intraoperative use of the gamma probe, following inspection of the well trained teams to remove the sentinel node(s) in about 10 minutes [43], [44].

However, a gamma probe can only provide count rate display and variable-pitch audio output based on the local activity concentration. In addition, SLN detection with both the large FOV camera and gamma probe (GP) can be incomplete. The false negative rate in SLNB is reported to be 5% to 10% [35], [36]. It is possible that such performance can be improved upon and the process simplified by using technology that will allow intraoperative

visualization of the activity distribution in the anatomic region of interest. For these reasons research has been undertaken to develop intraoperative imaging tools that can be used in the operating theatres to help the surgeons[43], [44].

II. Contemporary Small Gamma Cameras (SGC)

SGCs have been used for sentinel lymph node imaging and in acquiring biopsies of different types of cancer: breast cancer[45]–[47], gastrointestinal cancer [48], laryngeal cancer[7], oral cancer[49], [50], prostate cancer[51], renal cell carcinoma[52], testicular cancer[52], [53], malignant melanoma[50], [54], and gynecologic cancer [55].

Scopinaro *et al.* developed a small gamma camera (SGC) with 1 inch square field of view (FOV) [44]. The initial evaluation study aimed at demonstrating that intra-operative detection and surgical removal of mammary SLNs is quicker and more accurate when using the SGC and GP (gamma probe) together than when using the GP only. The study enrolled 120 consecutive patients with T1 breast cancer of the superior lateral breast quarter and clinically negative nodes, who had been scheduled for breast conserving surgery with SLN biopsy.

The SGC used for the study was a portable high resolution camera especially designed for radio-guided surgery. Its detector weighs about 1 kg and can be handheld during the operation. It is composed of a pure tungsten collimator with CsI(Tl) crystals inserted into its holes, a 1 in² FOV position sensitive photomultiplier tube (PSPMT), homemade readout electronics followed by ADCs, and a notebook computer serving as the acquisition console, display, archive, and data processor for image revision. The spatial resolution was calculated to be 3 mm at 1 cm distance from the source with an energy window of 10% centered at the 140-keV peak.

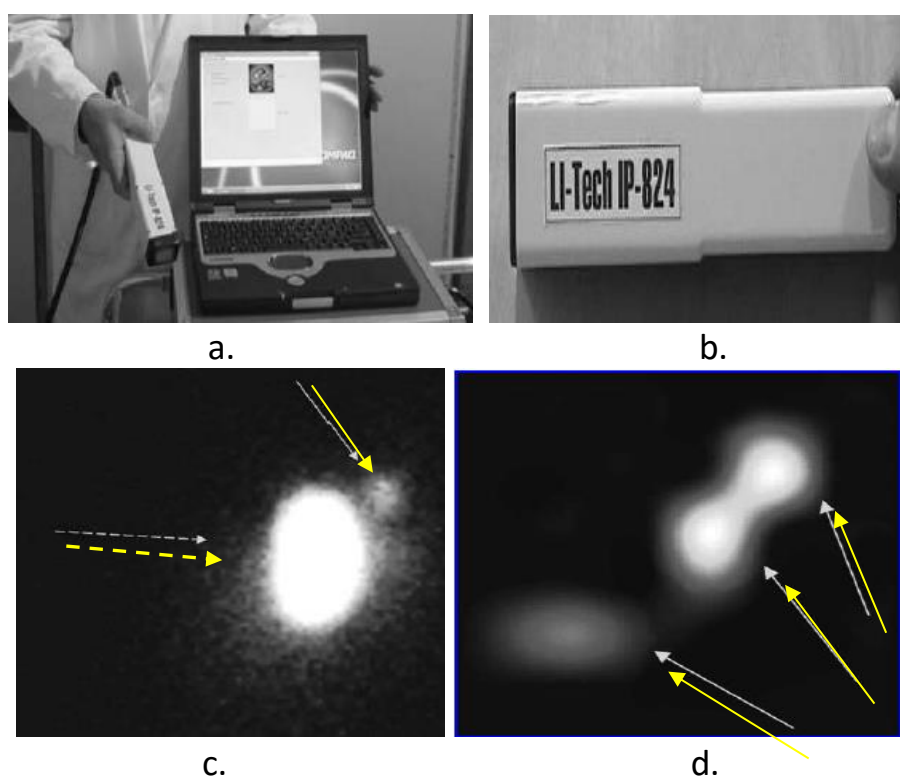


Figure 2-1: a. Photo of the camera and control computer used in the study of reference [44]; b. the detector alone; c. conventional large FOV Anger camera image showing a single node (solid arrow) and the injection site (dashed arrow); d. SGC image correctly showing 3 SNs (solid arrows)

The study showed that using the SGC, a larger number of sentinel nodes was found. Figure 2-1 shows the SGC used in this study. All the three SLNs were clearly seen while using the SGC whilst only one SLN was visible in case of Anger camera image. When considering patients with more than one SLN, average biopsy time was much shorter when both the SGC and the GP were used (6.0 minutes \pm 2.8 minutes) than in cases where only the GP (10.29 minutes \pm 4.9 minutes) was used [44].

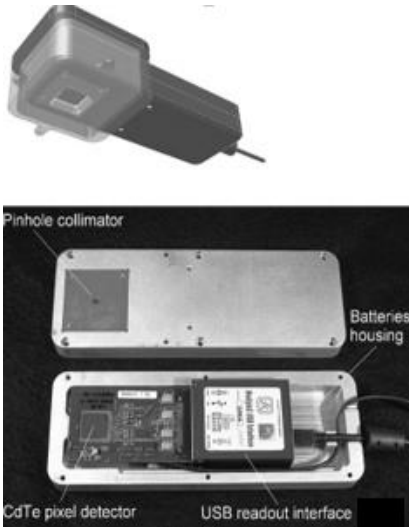
Tsuchimochi et al. have described several developmental and commercially available SGCs [43]. Some of them are shown in Figure 2-2. Table 1 lists a number of SGCs along with some of their physical characteristics. Table 2 compares the performances of these SGCs on the basis of metrics like spatial resolution, energy resolution and sensitivity.



a.



b.



c.



d.

Figure 2-2: a. The Small CdTe Gamma Camera system is composed of: detachable detector head which is mounted on the articulating arm, control unit, and power supply on the mobile cabinet; b. Minicam II camera head (CdTe detector); c. (top) Bottom view of the MediPROBE head, c. (bottom) Open view of the disassembled MediPROBE compact gamma camera head without the lead shield; d. MediPROBE mounted on an articulating arm [43].

Table 1: Characteristics of small gamma cameras [43]

Small gamma camera	Detector	Matrix size	FOV (detector)	Size (detector head)	Weight (with collimator)	Energy range	Collimator
POCI [2]	YAP (Ce), IPSD		Φ 24 mm		2 kg	Tc-99m, I-125, In-111	Parallel-hole
Minicam [®]	CdTe	16 × 16	49 mm × 49 mm	Φ 95 mm height 150 mm		20–200 keV	Parallel-hole
MinicamII [®]	CdTe	16 × 16	40 mm × 40 mm	70 mm × 170 mm × 250 mm	700 g ^a	30–200 keV	Parallel-hole
LumaGEM [®] [3]	CsI (Na) PS-PMT	16 × 16	20 mm × 20 mm			30–300 keV	Parallel-hole, pinhole
eZ-SCOPE [®] [4]	CdZnTe	16 × 16	32 mm × 32 mm	60 mm × 60 mm × 220 mm	800 g ^a	71–364 keV	Parallel-hole, pinhole, coded ap.
Second POCI [6]	CsI (Na) IPSD	50 × 50	Φ 40 mm	Φ 95 mm height 90 mm	1.2 kg	105–175 keV	Parallel-hole
Sentinella 102 [®] [13]	CsI (Na) PS-PMT	300 × 300	40 mm × 40 mm	8 cm × 9 cm × 15 cm	1 kg ^a	50–200 keV	Pinhole
GE camera [10,15]	CdZnTe	16 × 16	40 mm × 40 mm	Height 150 mm	1.2 kg ^a	40–200 keV	Parallel-hole
CarollReS [16,17,23]	Gd ₂ SiO ₅ (Ce) PS-PMT		50 mm × 50 mm	78 mm × 78 mm × 275 mm	2.49 kg		Parallel-hole
Imaging probe [59]	CsI (Tl) PS-PMT	20 × 20	49 mm × 49 mm		2 kg		Parallel-hole
MediPROBE [29,37]	CdTe	256 × 256	14.08 mm × 14.08 mm	200 mm × 70 mm × 30 mm	1.5 kg ^a		Pinhole
SSGC proto-type [7,26]	CdTe	32 × 32	44.8 mm × 44.8 mm	152 mm × 166 mm × 65 mm	2.7 kg	550 keV maximum	Parallel-hole
SSGC clinical-type [27]	CdTe	32 × 32	44.8 mm × 44.8 mm	82 mm × 86 mm × 205 mm	1.4 kg ^a	550 keV maximum	Parallel-hole

GE Camera = Intraoperative Gamma Camera, SSGC = Small CdTe Gamma Camera, coded ap = coded aperture collimator.

^a Without collimator.

Table 2: Performance of small gamma cameras [43].

Small gamma camera	System spatial resolution (FWHM) Tc-99m	Energy resolution (FWHM), Tc-99m	Sensitivity, on detector surface with collimator, Tc-99m
POCI [2]	1.9 mm at 0 cm	38%, Co-57	200 cps/MBq
Minicam [®]	5% (5%, Co-57)		
MinicamII [®]	2.46 mm, theoretical	5–7%	
LumaGEM [®] [3]	2.1 mm, 2.6 mm, at 0 cm, 3 cm	>20%	
eZ-SCOPE [®] [4]	2.3, 8.0, and 13.6 mm at 1, 5, and 10 cm	8.6%	184 cps/MBq
Second POCI [6]	3.9, 4.8, and 7.6 mm at 1, 2, and 5 cm	32%	290 cps/MBq
Sentinella 102 [®] [13]	5.4–8.2 mm, 7.3–11.0 mm, and 10.0–18.0 mm ^a at 3, 5 and 10 cm	15.9%	90–900 and 27–72 cps/MBq ^a , source-to-aperture distance, 1 and 10 cm
GE camera [10,15]	5 mm at 5 cm	8%	100 cps/MBq
CarollReS [16,17,23]	10 mm at 3 cm	45%, Co-57	1000 cps/MBq, theoretical
Imaging probe [59]	2.2 mm, intrinsic	20%	210 cps/MBq
MediPROBE [29,37]	5.6–12.6 mm ^b at 5 cm		6.5–33 cps/MBq ^b source-to-aperture distance, 5 cm
SSGC proto-type [7,26]	1.6, 3.9, 6.3, and 11.2 mm at 0, 2.5, 5.0, and 10.0 cm	7.8%	300 cps/MBq
SSGC clinical-type [27]	1.5, 2.3, 3.4 and 6.8 mm at 0, 2.5, 5.0 and 10.0 cm	6.9%	150 cps/MBq (high-resolution collimator)
	3.3, 6.9, 10.6 and 19.9 mm at 0, 2.5, 5.0 and 10.0 cm	6.9%	1600 cps/MBq (high-sensitivity collimator)

GE Camera = Intraoperative Gamma Camera, SSGC = Small CdTe Gamma Camera, coded ap = coded aperture collimator.

^a Pinhole apertures of 1.0, 2.5, and 4.0 mm.

^b Pinhole effective apertures of 0.94, 1.2, and 2.1 mm.

III. DeclipseSPECT system

The declipseSPECT system is an FDA-approved 3-D imaging system designed to be used pre-, post- and intra-operatively with a gamma probe in surgical application in which localized accumulation of a radiotracer can be anticipated, such as SLNB or tumor excision using tumor-targeting radiotracers. It consists of an optical/infrared tracking system, a trackable gamma probe and fast image reconstruction software.

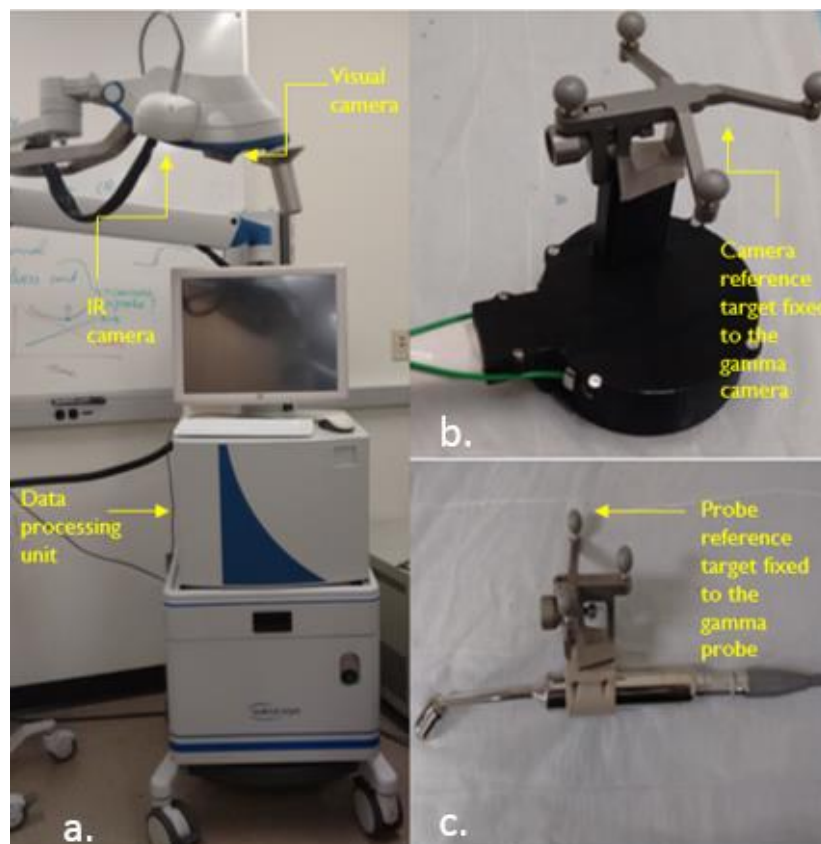


Figure 2-3: a. The declipseSPECT system; b. hand held gamma camera with the optical tracking system; c. gamma probe with the optical tracking system fixed on top

A second reference target with attached I-Spheres is adhered to a part of the patient that will not be moved during the image acquisition procedure and acts as a reference frame for calculating the position of the probe I-Spheres. The IR cameras are equipped with an IR light source that illuminates the surgical FOV. The reference targets permit 3 or more I-Spheres to be rigidly attached to the probe or patient, permitting precise determination of their position and orientation.



Figure 2-4: The reference targets that make up the optical tracking system

During a DeclipseSPECT scan the probe is scanned by the surgeon using the following protocol. The system is set up and the position of the tracker and optical camera iris adjusted for a good view of the patient by the surgeon. The

patient is roughly scanned while monitoring the count rate by listening to the audio output from the probe control box (Dilon Navigator2.0 gamma probe) and the flowing bar graph at the top of the screen on the declipseSPECT system. After the initial localization of basins containing hotspots in this manner, 3-D scan is performed for the small region of interest (ROI). During the 3-D scan, the probe is kept over the ROI, pointing towards the suspicious area as established from the rough scan till at least 600 counts are registered on the system. This is followed by changing the probe position to a plane perpendicular to the previous plane of scanning and letting another 600 counts to be registered on the system. This is repeated to make sure that probe is scanned over three perpendicular planes thus giving 3-D information with respect to the suspicious lesions.

Count rates from the probe are streamed to the system computer during the hand-held scanning procedure. The probe's location and orientation, along with the counting rate, are recorded and stored by the system. The resulting time series data are fed to an iterative reconstruction algorithm, which calculates the 3-dimensional distribution of the isotope within the system's FOV.

Over the past two years, a partnership among UVa, Dilon Technologies, SurgicEye, and the Jefferson Lab has interfaced a hand held gamma camera to

the data acquisition and image reconstruction components of the DeclipseSPECT system. The camera can be used as an alternative to the gamma probe. The potential advantages of replacing the non-imaging probe with a camera include the estimation of shape, extent and depth of the radiotracer uptake from the reconstructed images, better detection of sentinel lymph nodes in complicated situations like anatomic location of the nodes or proximity to the high-activity injection site and the ability to visualize the lesion area pre-incision thus improving the false negative rate associated with the gamma probe [56]. The evaluation of the 3D hand held gamma camera is the main object of this thesis and will be discussed in detail in the following chapters.

The small hand held gamma camera consists of a pixelated thallium doped sodium iodide (NaI(Tl)) scintillator, an array of 80 silicon photomultipliers (model S10362-33-050P from Hamamatsu Photonics, Hamamatsu, Japan) and a two-layer custom-built parallel-hole collimator. The crystal is 6 cm in diameter and 6 mm thick and is in a hermetically sealed package with a 1 mm thick glass window, a 0.5 mm aluminum entrance window, and with an overall package diameter of 7.5 cm and height of 9.5 mm. As described in *Popovic et al.* the MPPCs (Multi-Pixel Photon Counter) or SiPM (Silicon Photomultipliers) are arranged in a circular pattern with a central square array bounded on each side

by another array, giving a circular field of view with a 60 mm diameter. As shown in Figure 2-5d, a square region of 17 x 17 crystals makes the actual imaging region. This is because the response function (detector response to the radiations) is uniform in this region allowing standard techniques like crystal mapping, energy calibration and flood correction to be incorporated in the application program interface for the image processing software.

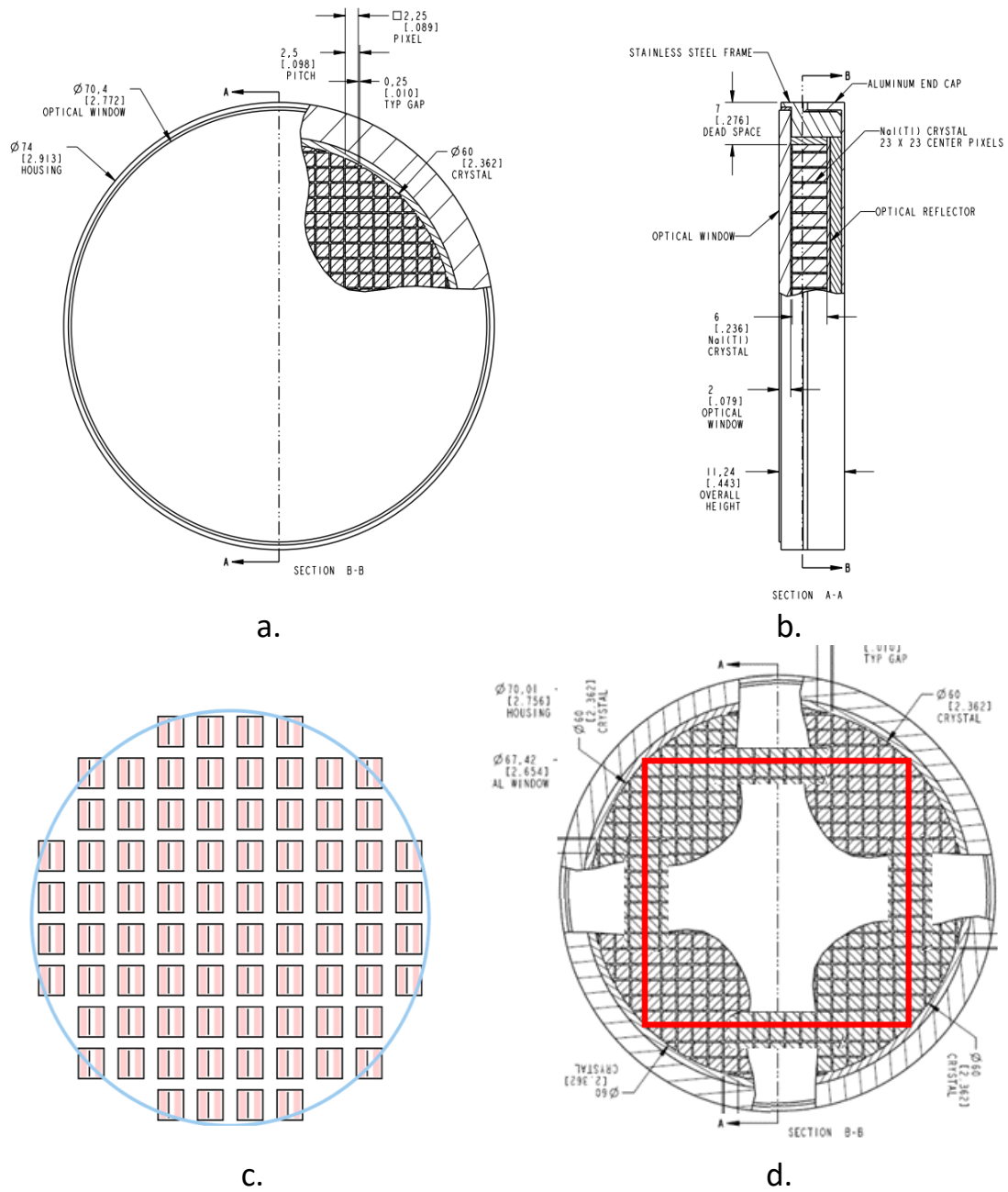


Figure 2-5: a. Camera specifications top view; b. camera specifications side view; c. arrangement of the 80 SiPMs; d. red square showing 17 x 17 crystal region used for imaging.

Reference: FreeHand SPECT with a Hand-Held Imager by Benjamin L. Welch, 2014 IEEE Medical Imaging Conference, Seattle, Washington, November 12, 2014

The disk-shaped camera housing is 75 mm in diameter, approximately 40.5 mm thick and has a mass of only 1.4 kg, permitting either hand-held or arm-mounted use. The scintillator is coupled to the MPPC array using a polydimethylsiloxane (PDMS) coupling compound to improve the scintillation light transfer to the MPPCs and insure a sturdy coupling. All camera components are integrated on a mobile cart that allows easy transport. The camera is designed to be used in surgical procedures, including determination of the location and extent of primary carcinomas, detection of secondary lesions, and sentinel lymph node biopsy (SLNB) [57].

This small gamma camera follows freehand SPECT imaging. Before starting the acquisition the camera is roughly moved over a broad region of interest and a real-time window that shows any hot spots as bright area against a black background is checked. These bright areas show the actual region of interest and thus is focused for the actual acquisition. Once this area is determined, the acquisition begins roughly for one minute. Scanning is followed by reconstruction using SurgicEye declipseSPECT software. The reconstructed image can be further filtered by focusing the region of interest and excluding the noise from this region. Once this process is done, which usually takes thirty

seconds, the reconstruction image is overlaid on region scanned with the help of the visual camera.

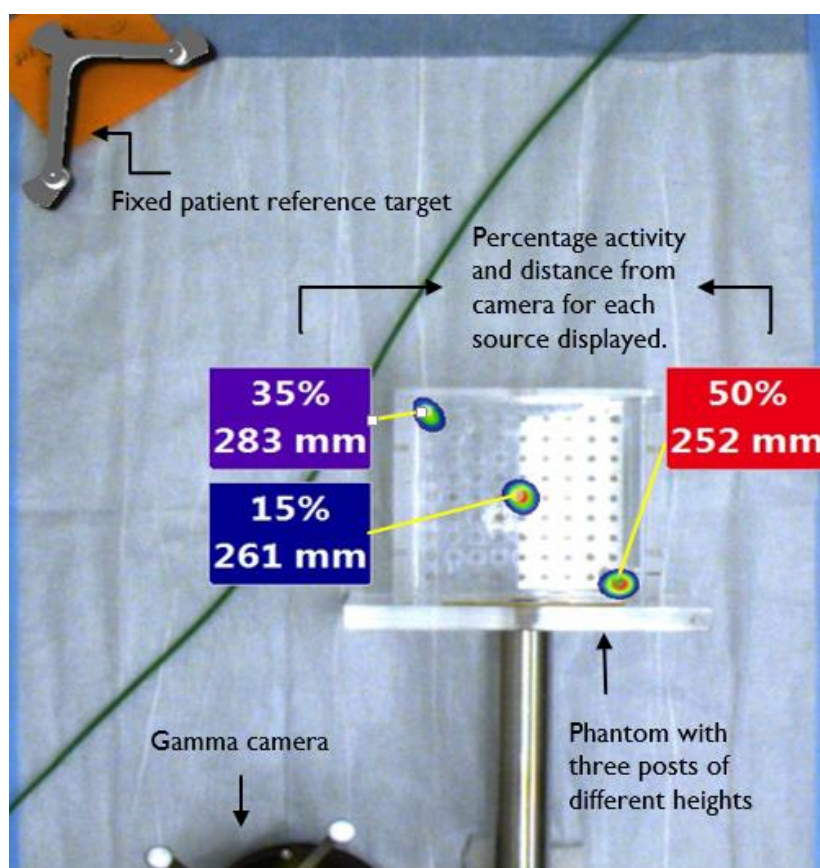


Figure 2-6: Reconstructed image overlaid on the phantom

A reconstructed image of a phantom with three posts having radioactivity on top is shown in Figure 2-6. By tracking the camera's location and orientation using the NIR cameras, the system can display the continuously updated separation between the camera surface and regions of reconstructed

focal radiotracer uptake (hotspots). As the camera is moved, the displayed distance changes, thus letting surgeons know the location of the hotspots in three dimensions relative to the camera. The software also calculates and displays the relative activities of each separate hotspot expressed as a percentage of the total activity within the reconstructed FOV of the system (see Figure 2-6).

The next chapter deals with characterizing this small gamma camera when operated in both 2-D and 3-D modes.

SYSTEM CHARACTERIZATION

I. Introduction

Every imaging system needs to be evaluated based on its basic imaging performance so that it can be used efficiently and capabilities and limitations during human imaging can be predicted. This process also enables identification of degraded performance, and troubleshooting to identify and correct the source. This chapter discusses imaging performance evaluation of the hand held gamma camera, used both in 2-D (scintigraphic) mode and in hand held SPECT (3-D) mode in conjunction with the DeclipseSPECT system [58].

A. Intrinsic Performance

The International Atomic Energy Agency describes two general types of gamma camera performance: extrinsic and intrinsic. Intrinsic performance is generally evaluated for component of the imager under ideal conditions. For gamma cameras, intrinsic performance is that with the collimator removed, and characterizes the detector alone [58].

B. Extrinsic performance

Extrinsic or system performance characterization is usually done for the entire nuclear medicine system under conditions that are clinically realistic. In case of gamma cameras, it is done with the collimator in place. For 3-D (SPECT) imaging characterization can include assessment of image quality in reconstructed images. The results of extrinsic performance measurements, when made with realistic phantoms, can be indicators of clinical performance and may provide useful information about system optimization for clinical studies.

In this thesis, all experiments were performed with the collimator on and hence all results will be descriptive of extrinsic or system performance [58].

II. Performance Evaluation

A. Energy Resolution

A.i) Background

The amplitude of the signal obtained from the camera is directly proportional to the energy deposited in the crystals by the γ -rays. The energy spectrum of the detected gamma rays is obtained by plotting a histogram of the detector pulse amplitudes. The shape of this spectrum depends on multiple factors including: the radiotracer emission spectrum, the amount of Compton

scatter, background radiation, and the characteristics of the energy conversion processes in the detector. For each emitted photon energy the energy spectrum contains a photopeak, corresponding to deposition of the entire photon energy in the detector. There is also a broader low energy region that indicates the incomplete deposition of γ -ray energy in the detector. This could also indicate Compton scattering of the γ -rays in the object containing the tracer leading to energy reduction before detection. An example energy spectrum is shown in Figure 3-1.

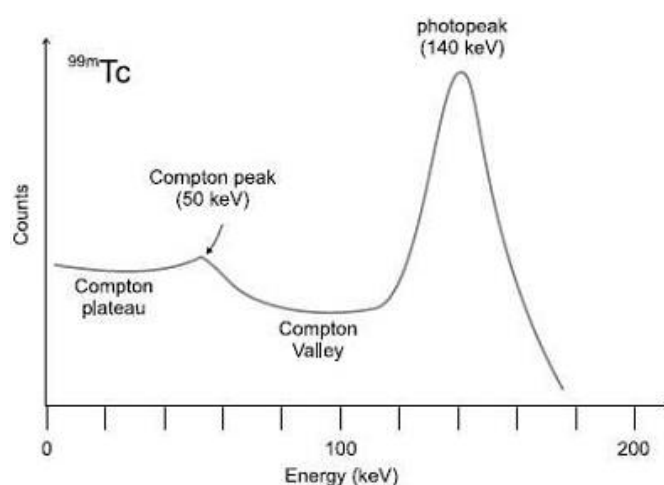


Figure 3-1: Energy spectrum of ^{99m}Tc

Reference: <http://oftankonyv.reak.bme.hu/tiki-index.php?page=Physical+processes+important+for+radiation+detection>

In nuclear medicine imaging, Compton interactions in the object being imaged or the camera's collimator degrade image quality because when the rays

scatter in the object they change directions, thus the information regarding the location of the original photon emission location is lost. The events with energies below those in the photopeak in the energy spectrum of Figure 3-1 are Compton events.

Energy resolution is a measure of the intrinsic ability of a detector to distinguish γ rays of different energies. The energy resolution of a detector is typically defined by the full width of the photopeak at one half of its maximum amplitude, divided by the energy of the photopeak, and is typically expressed as a percentage.

As the width of the spectral photopeak increases, the detector's ability to differentiate between γ rays whose energies are close to each other deteriorates. Thus a smaller energy resolution is desirable. The reason that energy resolution decreases at lower energies is greater statistical fluctuation in the measured signal. This greater fluctuation is either because of detection of fewer photoelectrons (in scintillation detectors with PMTs) or creation of fewer e-h pairs (for semiconductors). In addition, slight differences in operating characteristics between detectors can degrade the total energy resolution of a complete imaging system as compared to that of small individual detectors unless they are corrected for.

A.ii) Materials and methods

To measure the energy resolution of the hand held gamma camera a petri dish of diameter 85 mm covering the entire field of view of the camera was used. It was filled with ~ 1 mCi of ^{99m}Tc -pertechnetate forming a thin layer in the petri dish and acting as a low-scatter flood source. This flood source was placed on the gamma camera to obtain a high statistics flood image. The FWHM of the photopeak in the resulting whole-FOV energy spectrum was calculated using MATLAB programming language. The measurement was repeated seven times to reduce the statistical error, and the FWHM energy resolution was calculated for each trial.

A.iii)Result

The average energy resolution was calculated to be 21.5 ± 1.67 % (mean \pm 95% confidence interval) at 140 keV. A good energy resolution is important since this establishes how narrow the energy window can be that determines which detected events are kept. The energy window is usually centered on the photopeak and events falling outside the window are rejected.

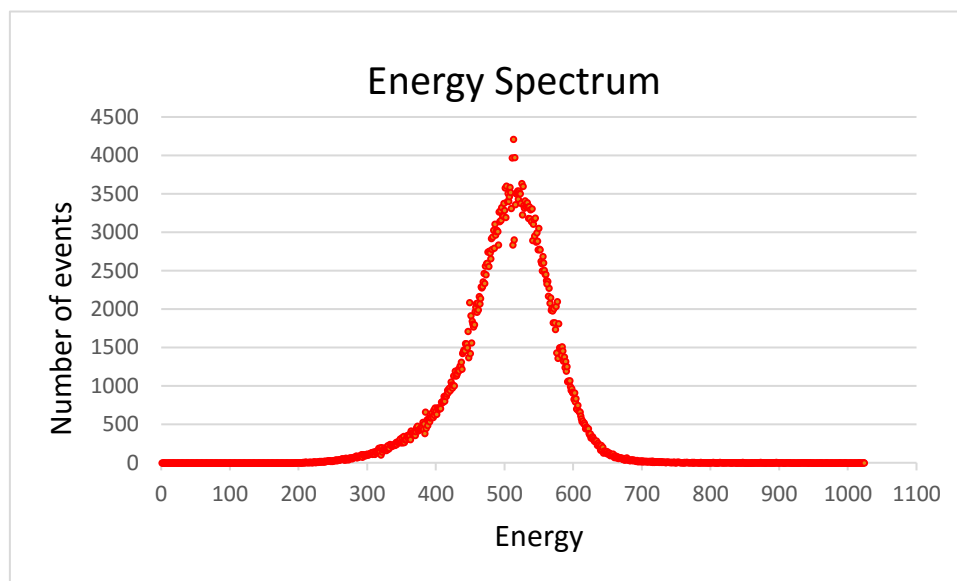


Figure 3-2: Energy spectrum

These scattered rays can reach the detector and provide incorrect information regarding their locations of origin, thus producing noisy, low contrast images. However because scattered photons have reduced energy a tight window around the true photopeak will help in ignoring them and obtaining a better quality image.

B. Spatial Resolution – 2D

B.i) Background

Spatial resolution describes the system's ability to differentiate between regions of radioactivity lying close to each other spatially. A single source of

activity might appear to be spread over multiple pixels close to each other, thus producing a blurring effect. Apart from blurring effect of small structures and edges, poor resolution also decreases the contrast of small structures relative to the surrounding background. This is caused by the object images being spread into the nearby background. Thus differentiation between areas of increased and decreased uptake might also become difficult.

The primary determinants of gamma camera spatial resolution are the detector's intrinsic spatial resolution and the geometric collimator resolution. The latter is a function of the source-to-collimator separation. For a parallel hole collimator the geometric spatial resolution, R_c is determined by length of the holes L , the hole diameter d and the source to collimator distance z as

$$R_c = d \cdot \frac{(L + z)}{L}$$

The relationship between the detector and collimator spatial resolutions and the overall (extrinsic) gamma camera resolution R_e is determined by R_c and the intrinsic resolution R_i as

$$R_e = \sqrt{R_i^2 + R_c^2}$$

This equation shows that except at very small source-to-collimator separations the collimator is the primary factor determining the spatial

resolution. Intrinsic resolution R_i refers to how well the crystal and PMT system localize an interaction in the crystal. It is affected by crystal thickness, gamma ray energy and scatter in the crystal.

When detectors with pixelated crystals are used, the spatial resolution of the system is limited by the pixel size. Spatial resolution is also affected by the energy of the photon and efficiency of collection of the scintillation light by the photomultipliers, with a greater number of photoelectrons leading to improved resolution in PSPMT-based cameras.

In this study, only the extrinsic spatial resolution was measured. It was calculated by measuring the full width at half maximum (FWHM) of the image of a thin line source.

B.ii) Materials and Methods



Figure 3-3: a. The experimental setup consisting of an angled capillary; b. the image obtained from the acquisition displayed using Image J

The thin line source was created using a small capillary tube (Kimble 71900-50 μL , 1 mm inner diameter). This capillary was filled with $^{99\text{m}}\text{Tc}$ -pertechnetate and translated from the surface of the camera (0 mm) to 100 mm away from the plane of the camera surface, obtaining images at every 10 mm in this range. From the captured images, the line spread function (LSF) at each source distance was found using Image J. The FWHM of the LSF is a measure of the spatial resolution of the system. This dependence of the FWHM of the LSF on source distance is important clinically, since nodes will be found at various depths inside the tissue.

B.iii)Result

Figure 3-4 shows the mean FWHM at various source to collimator distances with error bars depicting the standard deviation of the data values from the mean. Table 3 gives the mean spatial resolution \pm 95% confidence interval at source to collimator distances ranging from 0 mm to 100 mm.

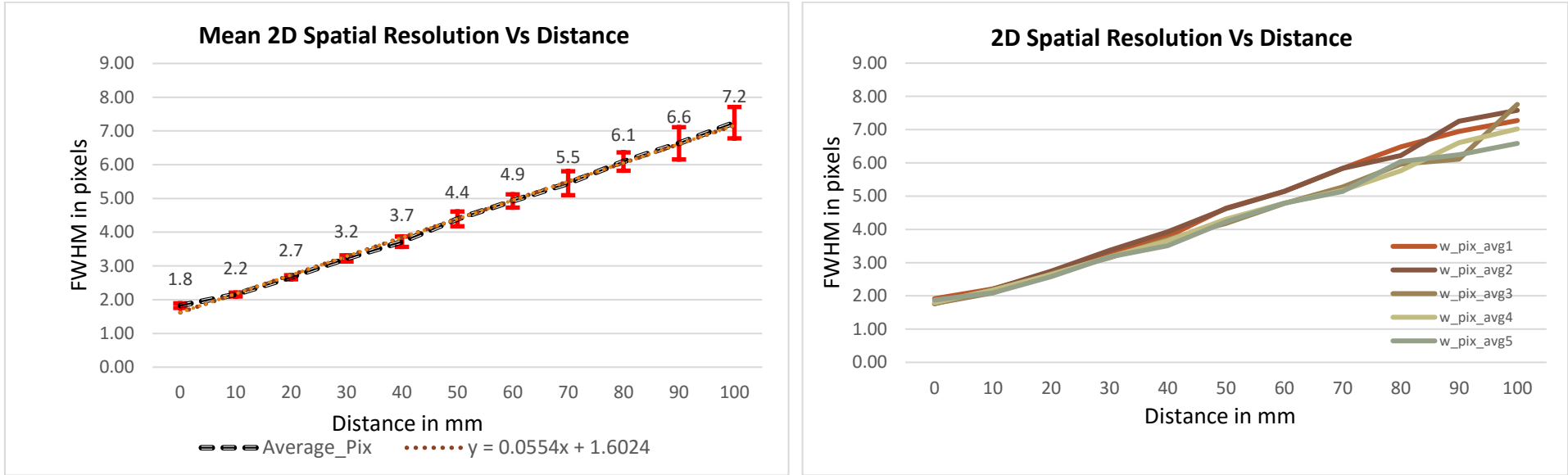


Figure 3-4: Mean Spatial resolution 2D vs Distance with bars indicating standard deviation.

Table 3: Mean spatial resolution with 95% confidence interval

Distance (mm)	0	10	20	30	40	50	60	70	80	90	100
Spat Res (pixels)	1.8 ± 0.07	2.2 ± 0.06	2.7 ± 0.06	3.2 ± 0.09	3.7 ± 0.2	4.4 ± 0.2	4.9 ± 0.2	5.5 ± 0.4	6.1 ± 0.3	6.6 ± 0.5	7.2 ± 0.5
Spat Res (mm)	4.6 ± 0.15	5.4 ± 0.13	6.7 ± 0.13	8.1 ± 0.20	9.3 ± 0.34	11.0 ± 0.48	12.3 ± 0.43	13.6 ± 0.78	15.2 ± 0.59	16.6 ± 1.0	18.1 ± 1.0

C. Spatial Resolution 3D

C.i) Background

Spatial resolution in 3-D mode is similar to the spatial resolution 2-D defined above, the difference being that this parameter is calculated in the reconstructed image produced by the SurgicEye reconstruction software, rather than in the projection images from the camera.

C.ii) Materials and Method

Four capillary tubes (Kimble 71900-50 μL , 1 mm inner diameter) filled with $^{99\text{m}}\text{Tc}$ -pertechnetate were placed so that separation distances of 5 mm, 10 mm, 15 mm and 20 mm were created. The capillaries were imaged in two coplanar perpendicular orientations, shown as position 1 and position 2, in Figure 3-5.

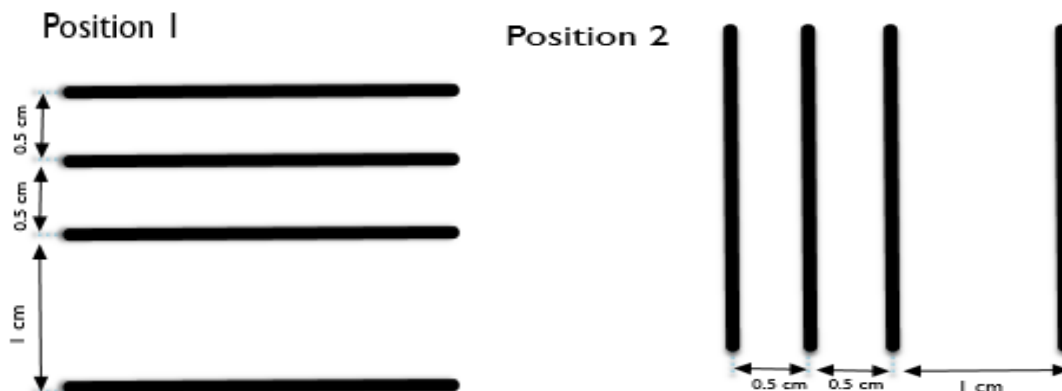


Figure 3-5: Experimental set up of capillary tubes for the calculation of 3-D spatial resolution

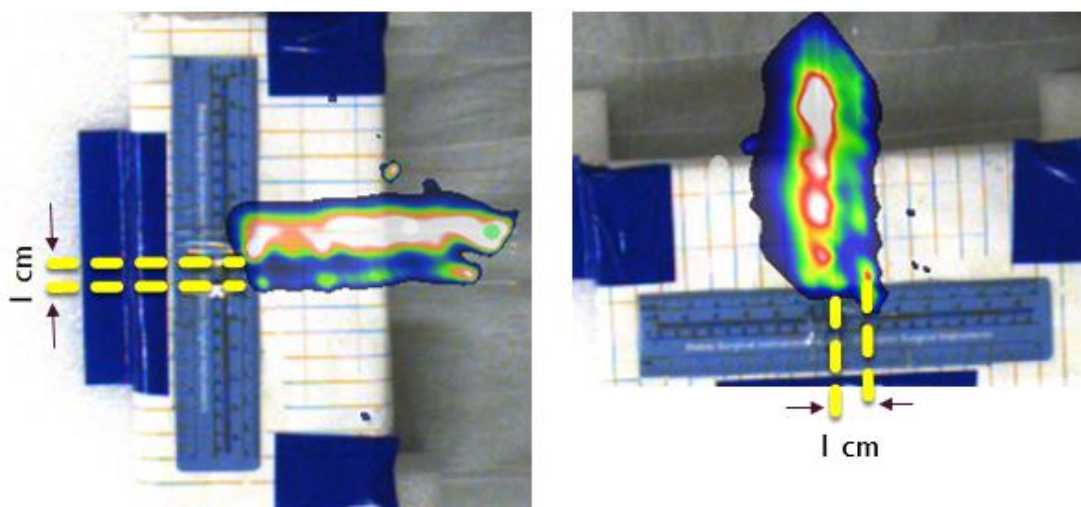


Figure 3-6: Reconstructed image in both positions 1 and 2 respectively.

Similarly, the spatial resolution in the third dimension was also measured. Two capillary tubes (Kimble 71900-50 μL , 1 mm inner diameter) were filled with $^{99\text{m}}\text{Tc}$ -pertechnetate and the separation between them was varied from 10 mm to 30 mm in 5 mm increments. The experimental setup is shown in Figure 3-7.

C.iii) Result

The reconstructed image was analyzed and checked whether the system could distinguish between the capillaries. From the reconstructed images, it is observed that the limiting spatial resolution 3-D is 10 mm, as seen in Figure 3-6 and Figure 3-8.

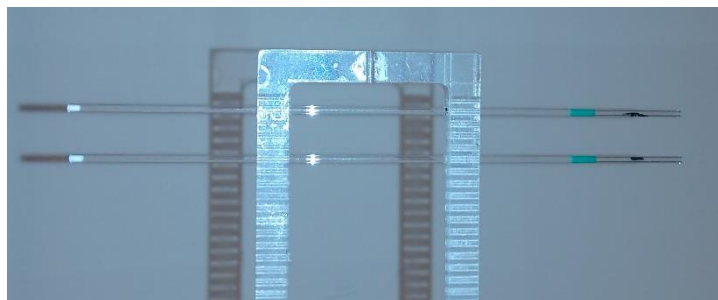


Figure 3-7: Experimental setup for finding spatial resolution in the third dimension

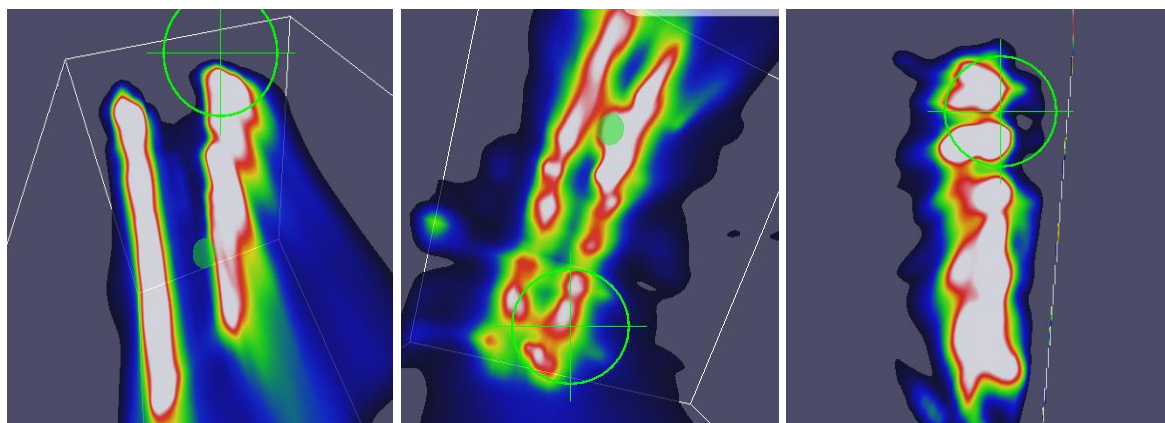


Figure 3-8: Reconstructed images of two capillaries at separation distances of (left) 25 mm, (middle) 15 mm and (right) 10 mm

D. Sensitivity – 2D

D.i) Background

Sensitivity of a gamma camera is typically expressed either as detected photons per emitted photons, or equivalently in detected counts per second per mega Becquerel of activity, describes how efficiently the camera is able to detect the incident radiation. Sensitivity depends on the geometric efficiency of the

collimator, the intrinsic photopeak efficiency of the detector, pulse height analyzer discriminator settings, and the dead time of the system [59]. The sensitivity has a direct impact on the radiotracer dose that must be injected into the patient and/or the total imaging time.

D.ii) Materials and Method

The sensitivity of the gamma camera was experimentally determined according to NEMA standards [60]. A flat bottomed petri dish with inner diameter of 10 mm was placed at 100 mm distance from the camera surface. A thin layer of ^{99m}Tc -pertechnetate was filled in the dish and image was acquired. Care was taken to make sure that the dish was placed at the center of the FOV, and that the entire periphery of the petri dish was visible in the image. The sensitivity at 100 mm separation between the camera and source was then calculated as the ratio of the total number of counts recorded in the image per second and the activity of the source.

D.iii) Result

This was calculated to be 170.67 ± 6.16 cps/MBq, where cps/MBq stands for counts per second per mega Becquerel. In Figure 3-9, the uniformity corrected image of the setup is shown.

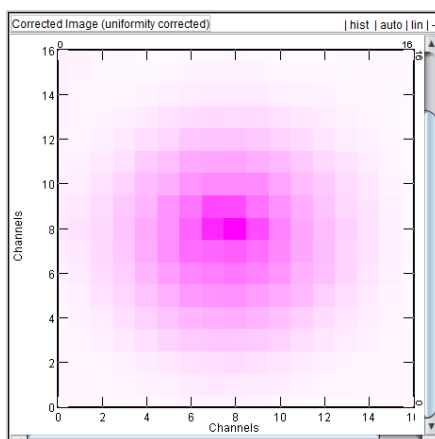


Figure 3-9: Corrected image of the 10 mm diameter petri dish at 100 mm from the camera surface

E. Sensitivity – 3D

E.i) Background

The 3-D sensitivity was based on the relative activities returned by the system reconstruction algorithm. Similar to 2-D sensitivity, 3-D sensitivity was defined as the ratio of total reconstructed image counts per second and the activity of the source when the distance between the source and the camera was 30 mm.

E.ii) Materials and Method

Eppendorf tubes were prepared with activities within the range of 3.59 μCi to 6060.27 μCi . The radioactive tube was then placed in the field of view of the gamma camera at a distance of 30 mm. This set-up was scanned with the gamma camera and the counts in each acquisition was noted down. The activity

sensitivity of the camera for each activity was then calculated as counts per second per activity and is plotted in Figure 3-10.

E.iii) Result

As can be seen in the Figure 3-10, the sensitivity is uniform in this range of activity with a mean sensitivity of 202.97 ± 19.51 cps/MBq.

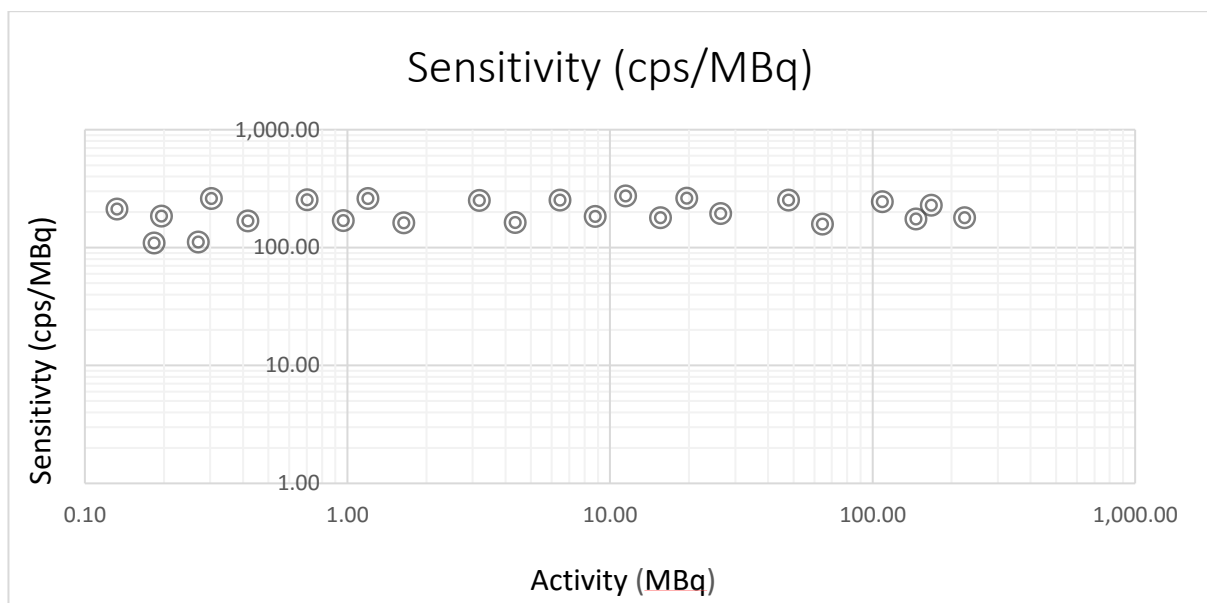


Figure 3-10: Plot of Sensitivity vs Activity

F. Depth Measurement

F.i) Background

In addition to providing the relative activity of the sources in the region of interest, the declipseSPECT software also tracks and reports the locations

these individual sources relative to the input surface of the gamma camera. Thus the distance of these sources from the camera can be obtained in real time after reconstruction of the image. Knowing the depth of the lesion provides the surgeons with useful information that could help them decide where to make the incision efficiently, or whether the depth of the node might be too great to justify its excision. This section describes experiments designed to test the accuracy of the distance measurement as reported by the system.

F.ii) Materials and Method

In this experiment, distance was defined as the separation between the camera collimator and the lesion. The true distance was measured using a ruler and compared to the distance displayed by the reconstruction software. Lesions were simulated using small spheres filled with average radioactivity of 25.71 μCi , and having activities varying from 18.18 μCi to 52.17 μCi . The first set of distance determination were obtained with the camera surface in contact with the lesions and hence the true distance is 0 mm in this case. Multiple scans were performed at this position and the distances were noted down. The second set was obtained with the distance between the camera surface and lesions being 35 mm.

F.iii) Result

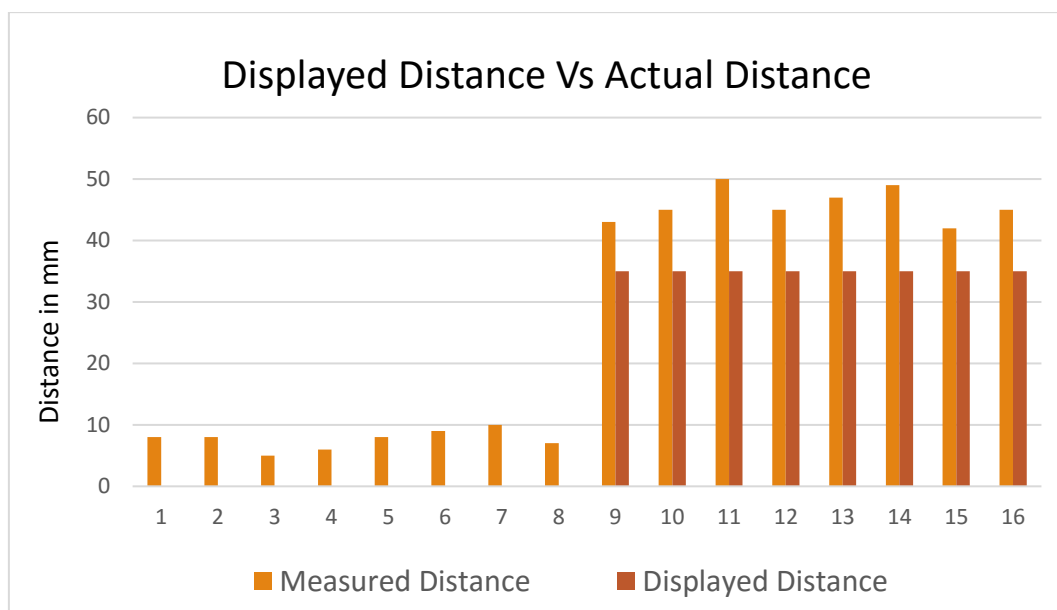


Figure 3-11: Plot illustrating the distance as measured by the system and the true distance for 16 cases.

Figure 3-11 summarises the data obtained from this study. It was observed that the distances as measured by the system had an average error of 9.19 mm with a standard deviation of 2.71 mm. This error can be explained by the fact that system displayed distance was from the source to the collimator of the camera. However, there is an outer camera covering with a thickness of ~9 mm to help with thermal insulation and electrical noise shielding. Thus it can be concluded that the distance as measured by the system corresponded well to the true values but with an offset of 9.19 mm.

G. Geometric Linearity

G.i) Background

In a SLNB procedure the nodes can be at any depth inside the tissue and they can be located in any arrangement among themselves, in the case of multiple nodes. A geometrically accurate imaging system should be able to return the spatial separations of the nodes without any geometric distortions; i.e. straight lines should be imaged as straight lines. This will provide surgeons with a good visualization of the lymphatic drainage system and help them in the surgical removal of sentinel lymph nodes.

G.ii) Materials and Method

To evaluate this characteristic of the camera, two wells of height 0.5 cm (A) and 2.5 cm (B) were placed on a box phantom with a separation distance of 2 cm between them. Point radioactivity $\sim 60 \mu\text{Ci}$ each was placed on top of the wells. This set-up was then scanned by the system and the reconstructed image was analysed.

Figure 3-12a shows the diagram of the lesions illustrating the dimensions of the wells and the separation between them. Figure 3-12b is the actual experimental set up. After the reconstruction, the system returns the distance between the camera collimator and imaged hotspots. The distance reported

changes the radioactive sources. Since the separation between the wells and the difference in their heights could be measured with a ruler, these two values were considered to constitute ground truth. The distances of the wells from the camera, obtained from 4 different viewing directions after one scan: side view 1, side view 2, front view and top view, were recorded.

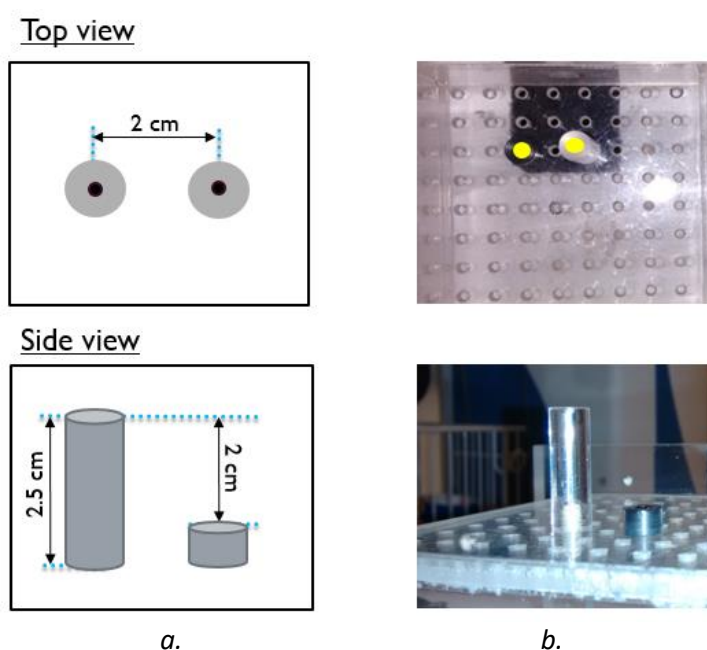


Figure 3-12: a. Representative experimental set up for evaluating the geometric accuracy of the system; b. real experimental set-up

In Side view 1, as shown in Figure 3-13, the camera was placed at three different locations and the distances of the radio-activities from the camera surface were recorded. Note that in these positions, the camera is always closer to the well A. Also, the separation between the two wells was 20 mm and

therefore the difference between the true distances of the two sources as measured by the system at each location should be 20 mm.

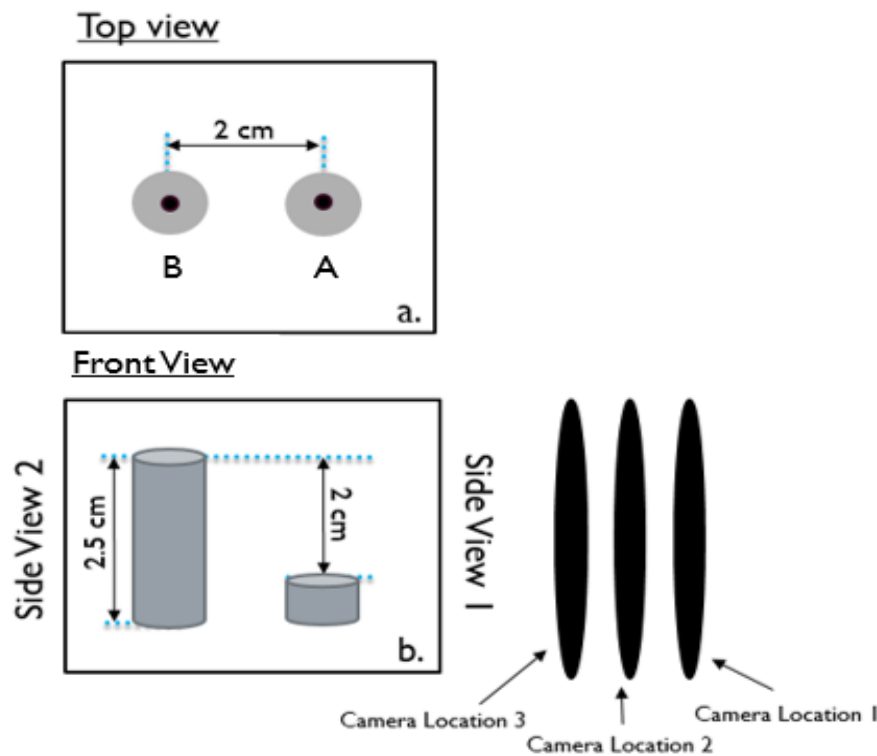


Figure 3-13: Experimental set-up illustrating the different camera locations and views

This was repeated for three other views as well. In side view 2, the camera will always be closer to well B and again the difference in the distances of the wells should be 20 mm. For the top view, the camera was again placed at three different locations. At every trial the difference between the distances of the two wells should be 20 mm since that is the difference in their heights. In front view, the two wells were in a plane parallel to the surface of the camera.

Hence they were at the same distance from the camera surface. Thus the difference in their distances as measured by the camera should be 0 mm.

G.iii) Result

Table 4: Observation table

Experiment:		Geometric Integrity			
Side View1		Trial 1 (mm)	Trial 2 (mm)	Trial 3 (mm)	TRUE Value (mm)
	Small Well (A)	120	119	117	
	Big Well (B)	141	139	137	
	Difference in Distance	21	20	20	20
Side View2		Trial 1 (mm)	Trial 2 (mm)	Trial 3 (mm)	TRUE Value (mm)
	Well A	174	73	175	
	Well B	155	54	157	
	Difference in Distance	19	19	18	20
Front View		Trial 1 (mm)	Trial 2 (mm)	Trial 3 (mm)	TRUE Value (mm)
	Well A	127	189	230	
	Well B	123	187	231	
	Difference in Distance	4	2	1	0
Top View		Trial 1 (mm)	Trial 2 (mm)	Trial 3 (mm)	TRUE Value (mm)
	Well A	75	135	70	
	Well B	53	115	50	
	Difference in Distance	22	20	20	20

Table 4 summarises the observations obtained from this experiment. From this data, error with which the system measures the distances of the radioactive sources from the camera from all the different views was calculated. The depth information of the lesions were accurately reproduced with a mean absolute error of 1.2 ± 0.34 mm (95% confidence interval).

H. Quantification of the Activity

H.i) Background

As mentioned in Chapter 2III. , the system reports the relative activity of the sources in terms of their percentage of the total activity imaged by the system in the region of interest. This measure is clinically significant because of the 10% rule followed by surgeons during sentinel lymph node biopsy. According to this rule, all nodes with radiation activities more than 10% of that of the hottest node and all blue dye stained nodes should be removed. Even though recent studies show that following this rule results in removal of a larger number of nodes than necessary, this is the current standard in hospitals [61], [62]. Thus an attempt was made to test how well this investigational imaging system can aide surgeons in making the decision about excision of nodes.

H.ii) Materials and Method

In this experiment, nodes were simulated using spheres of outer diameter 50 mm filled with radioactivity ranging from 1.78 μCi to 859.52 μCi . Sets of 2, 3 and 4 nodes were grouped together and scanned with the camera using the declipseSPECT software. Their relative activities as measured by the system were recorded. This was compared to the true relative activities of the sources calculated using their true activities (measured using Capintec CRC-15R dose calibrator).

H.iii) Result

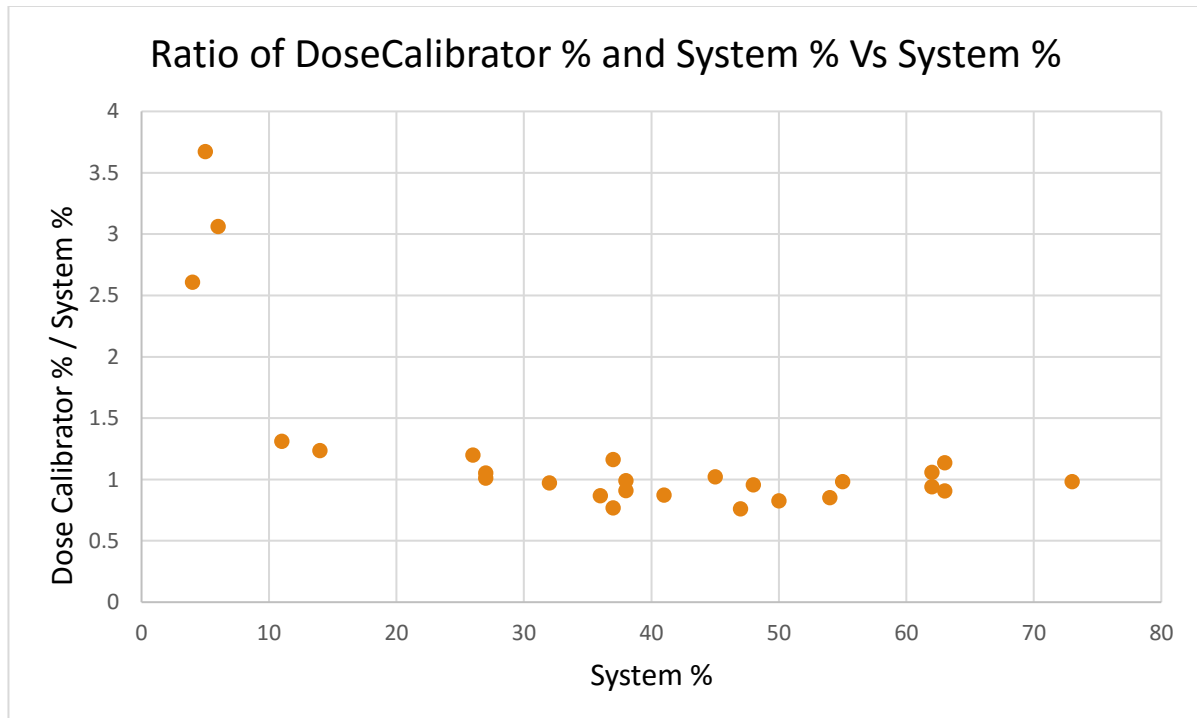


Figure 3-14: Plot of ratio of true % and observed % vs observed % of activity

In Figure 3-14, a plot of the ratio of true % activity and observed % activity against the observed % activity is shown. As can be seen, the ratio is close to 1 for relative activities in the range of 10% and onwards as seen by the system. This ratio deviates from 1 when the relative activity falls below 10%. Based on the data shown in Figure 3-14 it was determined that for nodes whose activity was more than 10% of the total activity in the scanned FOV, the system calculates the relative measures of radioactivity accurately with an average error of 18.0843% and standard deviation 20.1232%.

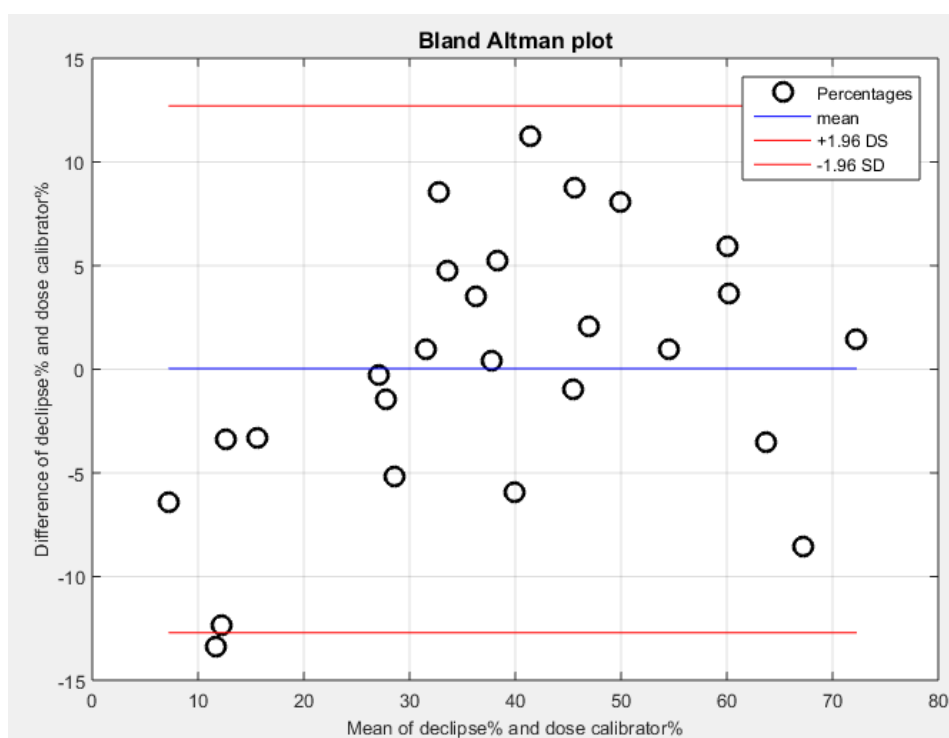


Figure 3-15: Bland Altman plot comparing the two techniques used to measure the relative percentage of the radioactive sources.

Figure 3-15 shows the Bland Altman plot comparing the two methods used for the quantification of radio-activities. Since the mean of the difference between observed % and true % is zero, there is no systematic bias associated with the reporting of the relative activities by the system. The sentinel node was correctly identified in each case with 100% accuracy.

I. Attenuation Correction

I.i) Background

Gamma rays emitted by a source (node or lesion) are attenuated (absorbed and/or scattered) by any intervening material between the source and the gamma camera. If a source is located deeper inside the tissue, the gamma rays reaching the camera will be attenuated more than the rays reaching the camera from a source located nearer to the camera in the same tissue. For example this is a problem in SLNB when determining relative node activity using a non-imaging probe, since deeper nodes appear to have lower activity than they truly have. The activity of the rays A_o coming out of a material with linear attenuation coefficient μ after travelling x distance in the attenuating material is given by Beer's law [63] as

$$A_o = A_i * e^{(-\mu x)}$$

where A_i is the activity of the rays before entering the material.

However, attenuation compensation can be built into 3D reconstruction algorithms if the attenuation of the intervening material is known or can be approximated. These tests were performed to evaluate the degree to which the investigational system's reconstruction algorithm can perform attenuation correction.

1.ii) Materials and Method

Two small spherical simulated lesions of average activity 24.5 μCi were placed in a box phantom at varying depths (separation = 20 mm) from the camera (see Figure 3-16). The camera surface is kept close to the box phantom surface. In position 1, L1 was at a distance of 20 mm from the camera surface and L2 was at 40 mm from the camera surface. This set-up was then scanned in 3D mode with the investigational system, first with no water in the box and next with water in the box. For the in-water case two trials were performed. In all cases the separation between the lesions was held fixed at 20 mm.

Following each scan the relative lesion activities calculated by the system were recorded. This is represented by 'System L1 percentage' and 'System L2 percentage' in Table 5. Activities of lesions at the time of acquisition were given by the quantities 'True L1 Activity' and 'True L2 Activity'.

In position 2, the lesion locations were exchanged and the procedure was repeated. Using the known lesion activities and the Beer Lambert law, the attenuated activities of these lesions, taking into account attenuation of the gamma rays as they pass through the air or water above them were calculated and given by 'L1 Apparent Activity' and 'L2 Apparent Activity', as shown in Table 5.

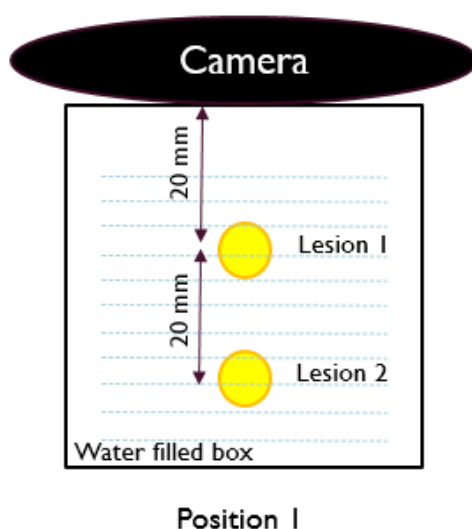


Figure 3-16: Experimental setup

1.iii)Result

Table 5 provides a summary of the data calculated in this experiment. The linear attenuation coefficient of air at 140 keV is 0.000167 cm^{-1} and that of water at the same energy is 0.1538 cm^{-1} . The true relative activities of the

lesions, expressed as percentages of their total activity were given by 'True L1 Percentage and 'True L2 Percentage. 'Apparent L1 Percentage and 'Apparent L2 Percentage were similar relative quantities but calculated using the Apparent L1/L2 activities. 'System L1 Percentage and 'System L2 Percentage were the percentages of the total activity calculated by the system for each lesion.

Table 6 shows that even though the lesions might deceptively look less radioactive than they actually were owing to the effect of attenuation caused by the water medium, the system compensated for this effect and correctly identified the higher (or lower) active sources. True L1 Percentage column shows the fraction of total activity actually contained in lesion 1, and that can be compared to System L1 Percentage to see how well the imaging system was able to perform attenuation correction. Similar comparisons can be made for L2. The percentage error in the system-reported fractional activities, relative to the known fractional lesion activities, is shown in the two rightmost columns.

Table 5: Data collected from the experiment. The true relative activities of the lesions, expressed as percentages of their total activity were given by 'True L1 Percentage and 'True L2 Percentage. 'Apparent L1 Percentage and 'Apparent L2 Percentage were similar relative quantities but calculated using the Apparent L1/L2 activities. 'System L1 Percentage and 'System L2 Percentage were the percentages of the total activity calculated by the system for each lesion.

In Air	True L1 Activity (μCi)	L1 Apparent activity (μCi)	True L1 Percentage (%)	Apparent L1 Percentage (%)	System L1 Percentage (%)	True L2 Activity (μCi)	L2 Apparent activity (μCi)	True L2 Percentage (%)	Apparent L2 Percentage (%)	System L2 Percentage (%)
Position #1	21.79	21.79	44.71	44.72	48.00	26.95	26.93	55.29	55.28	52.00
Position #2	21.54	21.54	44.71	44.72	42.00	26.64	26.62	55.29	55.28	58.00
In Water										
Position #1	21.29	15.65	44.71	52.38	33.00	26.33	14.23	55.29	47.62	67.00
Position #1	20.93	15.38	44.71	52.38	22.00	25.88	13.99	55.29	47.62	78.00
Position #2	20.93	11.31	44.71	37.28	43.00	25.88	19.03	55.29	62.72	57.00
Position #2	20.69	11.18	44.71	37.28	48.00	25.58	18.81	55.29	62.72	52.00

Table 6: Comparison of the relative activities as detected by the system to the true activities. The percentage error in the system-reported fractional activities, relative to the known fractional lesion activities, is shown in the two rightmost columns

In Air	True L1 Percentage (%)	True L2 Percentage (%)	Apparent L1 Percentage (%)	Apparent L2 Percentage (%)	System L1 Percentage (%)	System L2 Percentage (%)	System L1 % error	System L2 % error
Position 1	44.71	55.29	44.72	55.28	48.00	52.00	7.36	5.95
Position 2	44.71	55.29	44.72	55.28	42.00	58.00	6.06	4.90
In Water								
Position 1	44.71	55.29	52.38	47.62	33.00	67.00	26.19	21.17
Position 1	44.71	55.29	52.38	47.62	22.00	78.00	50.79	41.07
Position 2	44.71	55.29	37.28	62.72	43.00	57.00	3.82	3.09
Position 2	44.71	55.29	37.28	62.72	48.00	52.00	7.36	5.95

J. Effect of Injection Site

J.i) Background

During the sentinel lymph node biopsy, the radioactive colloid is injected using peri-tumoral, sub-dermal or sub-areolar injection techniques[64]–[67]. The drainage of the radioactive tracer from the point of injection then tracks the path of putative cancer cells through the lymphatic system. Since the injection is done in tissue and drainage is through the lymphatic system, drainage from the injection site to the sentinel nodes will take about 24 hours. The amount of injected activity that ends up in a sentinel node is only $3.5 \pm 3.1\%$ of the injected activity [9] so the injection site is considerably more radioactive than the nodes at the time of surgery. This significantly high radioactive source emits numerous gamma rays some of which can scatter into the parallel holes of the gamma camera collimator, producing background noise in the projection images.

J.ii) Materials and Method

To assess the degree of severity of this scatter radiation, the effect was simulated with an experimental set up shown in Figure 3-17. Case 1 consisted of two spherical radioactive node-simulating sources of approximately 4 μCi each, similar in activity to sentinel nodes. These sources were immersed in a water

filled box phantom to simulate nodes embedded in the tissue. Refer to Figure 3-17a.



Figure 3-17: Experimental setup with two cases to check the effect of scatter originating at the injection site; (a) without an injection site; (b) with an injection site outside the camera's FOV

These nodes were placed in the centre of camera's FOV and counts were acquired for 5 minutes. Next, in Case 2, one lesion of approx. 425 μCi activity, similar to the injected activity used at UVA for SLNBs, was taken to simulate the injection site. The two nodes and the injection site were immersed in the water filled box phantom. Only the two simulated nodes were placed in the centre of camera's FOV. Refer to Figure 3-17b. Care was taken to have the injection site outside camera's FOV. Again counts were acquired for 5 minutes. Table 7 clearly shows the increase in counts in both the image histogram and the change in shape of the energy spectrum due to the injection site in Case 2. Note the

additional lower energy counts in the second spectrum, which are from scatter originating at the injection site.

J.iii) Result

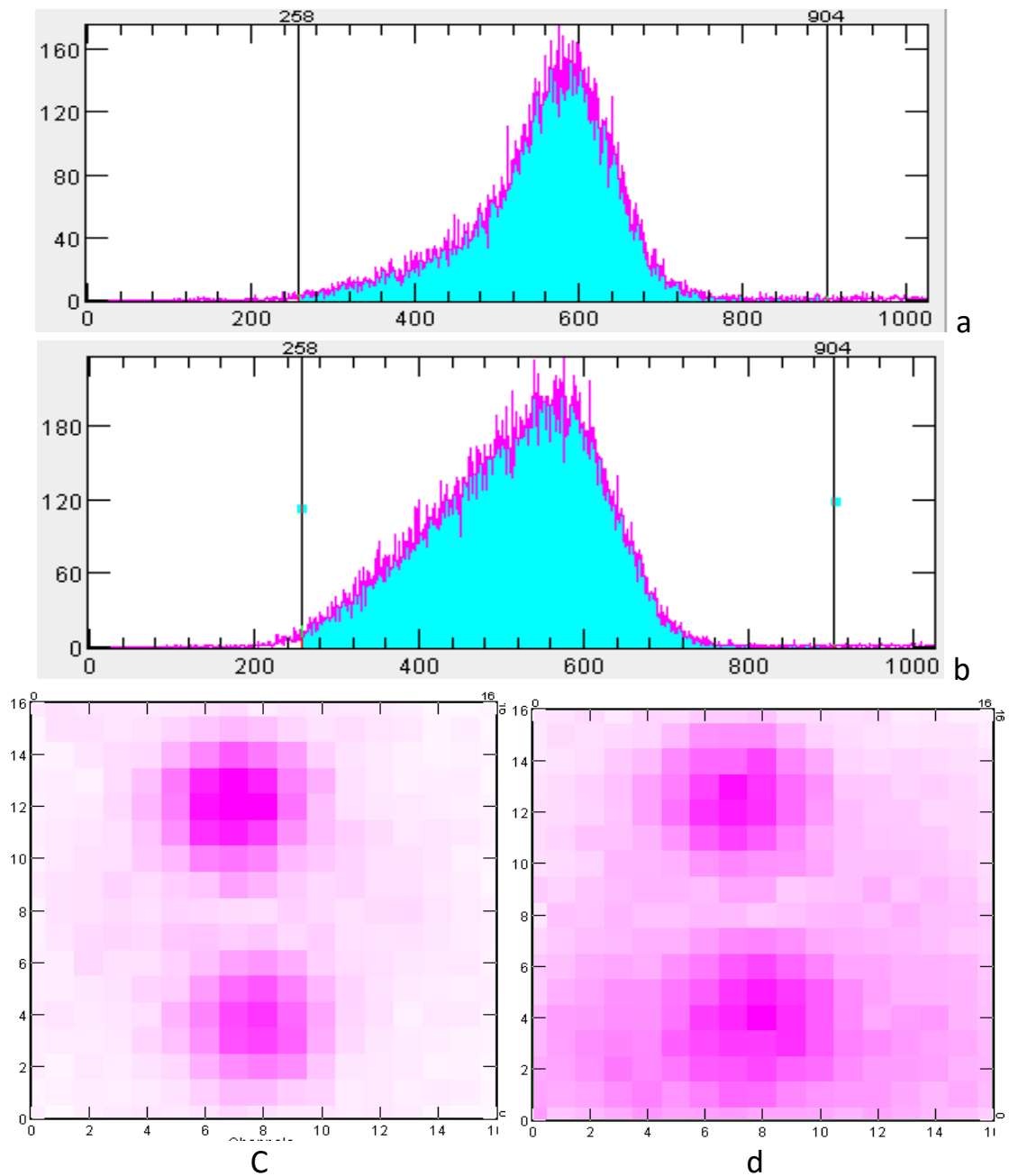


Figure 3-18: Effects of scatter due to injection site a. Energy histogram with no injection site present; b. energy histogram with injection site present; c. node images with no injection site; d. node images with injection site present.

Table 7: Summary of the total counts calculated in each case

Corrected Energy Sum			Corrected Image Sum		
W/o scatter	W/ Scatter	Difference	W/o scatter	W/ Scatter	Difference
25,918	49,202	23,284	25,821	48,251	22,430

Since the injection site (IS) causes a significant amount of scatter in the field of view (FOV) of the camera, the effect on the amount of detected scatter of the distance of the injection site from the nodes was investigated. For this experiment, the setup shown in Figure 3-19 was used.

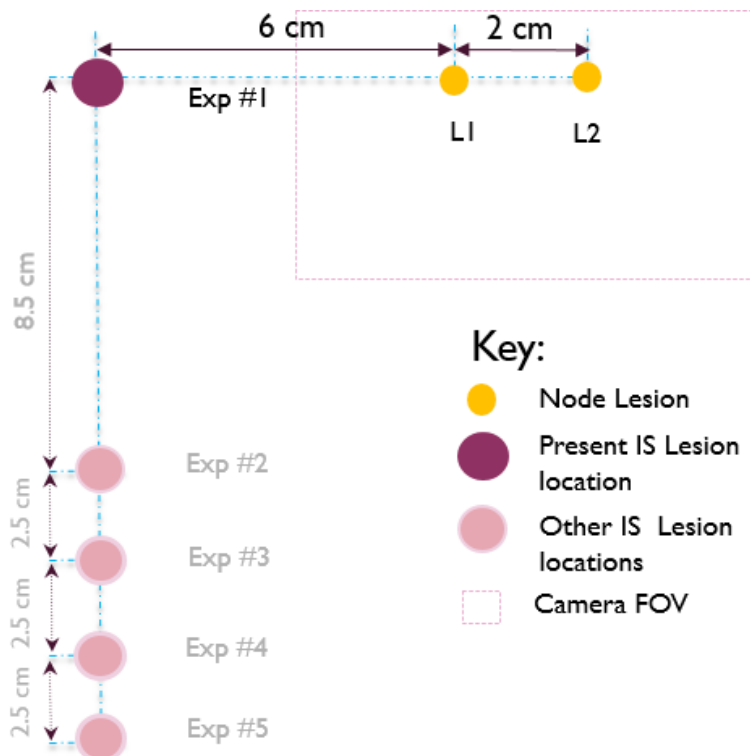


Figure 3-19: Experimental setup to check the effect of distance of IS from nodes

The perpendicular I.S. was varied from a distance of 85 mm to 165 mm and the counts in image histogram and energy curve were recorded. Figure 3-20 shows the percentage of scatter as a function of the total counts of the image histogram decreasing and reaching a constant value as the injection site is moved farther away from the node location.

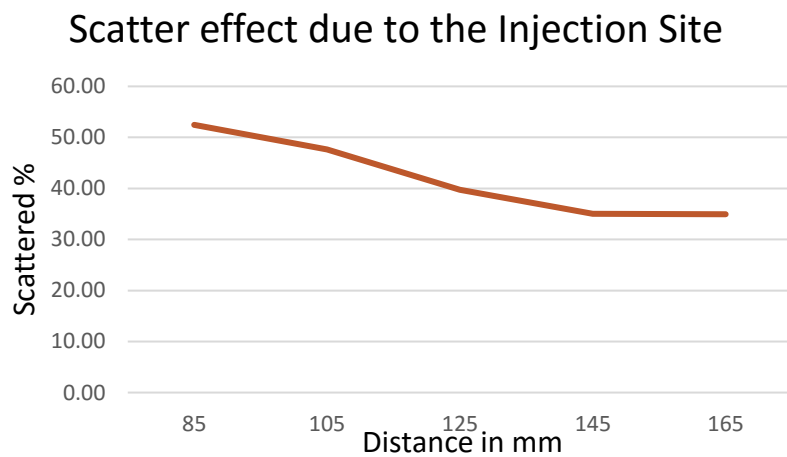


Figure 3-20: Plot showing the percentage of scatter observed in the uniformity corrected image with increasing distance from the nodes

CHAPTER 4

CONCLUSION

During surgical intervention, significant changes in tissue morphology and topology can occur. This will contribute to the higher false-negative rate (5-10%) than is generally recognized during SLNB. Intra-operative image guidance would provide real-time surgical guidance by providing anatomical and functional information about the operating site. This would provide in situ tissue structure and function characterization.

This thesis has explored whether the use of a 3-D intraoperative imaging system using a hand held gamma camera could provide advantages compared to the use of the non-imaging probe. The potential advantages of replacing the non-imaging probe with a camera include real time tracking of the changes in the morphology and topology of the tissues, the estimation of shape, extent and depth of the nodes and better detection of sentinel lymph nodes in complicated anatomic location of the nodes or close proximity to the high-activity injection site.

Compared to similar developmental and commercial small FOV gamma cameras, the gamma camera described in this thesis shows comparable or superior resolution and detection efficiency performance and in a hand-held comfortable package. The results from this study can be summarized to provide a better understanding of the performance of the novel hand held gamma camera.

The average energy resolution of the investigational gamma camera was calculated to be 21.5 ± 1.67 % (mean \pm 95% confidence interval) at 140 keV. This is higher than the energy resolution of small gamma cameras specified in Table 2.

An appreciable spatial resolution of 4.6 ± 0.15 mm at 0 mm source to collimator distance was calculated in 2-D mode. One of the widely used gamma probes in the hospitals of the United States of America, C-Trak Omni-Probe from Care wise has a spatial resolution of 15 mm at 10 mm source to collimator distance. Another gamma probe, ScintiProbe 15-B, pol.hi.tech has a spatial resolution of 20 mm at 10 mm source to collimator distance. These are considerably inferior to 5.4 ± 0.13 mm spatial resolution of the hand held gamma camera calculated at the same source to collimator distance. Spatial resolution of 1 cm was observed in 3-D mode.

Activity sensitivity in 2-D mode was recorded as 170.67 ± 6.16 cps/MBq and 202.97 ± 19.51 cps/MBq in 3-D mode. The gamma probes, due to their poor ability to reject scatter and pin-hole collimators have better sensitivity than the hand held gamma camera. Maximum sensitivities of C-Trak Omni-Probe from Care wise is 23000 cps/MBq and ScintiProbe 15-B, pol.hi.tech is 12000 cps/MBq.

The system preserves the geometric linearity of the object and gives the depth measurement accurately with a minor error of 1.2 mm. Attenuation effect due to distance of the lesions in a radiation attenuating material is accurately corrected by the system. Thus the system provides for the attenuation effect caused by the surrounding tissue. The sentinel nodes are detected by the system with 100 % accuracy but quantification of the detected activity has an error of 18.0843%. This parameter can be modified for a better quantification result by the system. Scatter from the injection site can affect the reconstructed images and consequently detection of sentinel lymph nodes. Hence care should be taken while scanning with the camera near the injection site.

This investigational system has several unique features and its evaluation shows that surgeons can obtain valuable information from its use during the surgery. This can be validated by conducting a clinical trial and analyzing the results.

CHAPTER 5

FUTURE WORK

Following the characterization of the system, next step is to use the system in the operating room (OR) for sentinel lymph node biopsy procedures and validate the results obtained in this thesis. The proposed study is designed to evaluate the new system for 3-D image guidance. The system will be used for locating sentinel lymph nodes (SLNs) following standard injection of radiotracer among melanoma patients. In addition to the investigational system two FDA-approved system for SLN mapping will also be used in the study:

- 1) FGC-probe (current standard of care): Pre-operative, 2-D imaging with a fixed gamma camera (FGC), followed by gamma probe used intraoperatively.

- 2) 3D probe: a novel FDA approved system that obtains 3-D images of the radiotracer using a scanning non-imaging probe (SurgicEye declipseSPECT) coupled to an FDA approved intraoperative gamma probe (Dilon 14 mm Navigator GPS). The working of this probe is explained in Chapter 2. The two systems (1 and 2) will be compared with the investigational hand held gamma

camera system to evaluate its usability in pre-surgical planning and intraoperative localization of sentinel node.

REFERENCE

- [1] “What Is Cancer?,” *National Cancer Institute*. [Online]. Available: <http://www.cancer.gov/about-cancer/understanding/what-is-cancer>. [Accessed: 08-Jun-2016].
- [2] “Cancer - Mayo Clinic.” [Online]. Available: <http://www.mayoclinic.org/diseases-conditions/cancer/basics/definition/con-20032378>. [Accessed: 08-Jun-2016].
- [3] A. F. Chambers, A. C. Groom, and I. C. MacDonald, “Metastasis: Dissemination and growth of cancer cells in metastatic sites,” *Nat. Rev. Cancer*, vol. 2, no. 8, pp. 563–572, Aug. 2002.
- [4] N. E. Tobler and M. Detmar, “Tumor and lymph node lymphangiogenesis—impact on cancer metastasis,” *J. Leukoc. Biol.*, vol. 80, no. 4, pp. 691–696, Oct. 2006.
- [5] S. A. Stacker, C. Caesar, M. E. Baldwin, G. E. Thornton, R. A. Williams, R. Prevo, D. G. Jackson, S. Nishikawa, H. Kubo, and M. G. Achen, “VEGF-D promotes the metastatic spread of tumor cells via the lymphatics,” *Nat. Med.*, vol. 7, no. 2, pp. 186–191, Feb. 2001.

- [6] "Lymph Nodes and Cancer." [Online]. Available: <http://www.cancer.org/cancer/cancerbasics/lymph-nodes-and-cancer>. [Accessed: 09-Jun-2016].
- [7] R. F. Uren, "Cancer surgery joins the dots," *Nat. Biotechnol.*, vol. 22, no. 1, pp. 38–39, Jan. 2004.
- [8] L. T. Dengel, M. J. More, P. G. Judy, G. R. Petroni, M. E. Smolkin, P. K. Rehm, S. Majewski, M. B. Williams, and C. L. Slingluff, "Intraoperative Imaging Guidance for Sentinel Node Biopsy in Melanoma Using a Mobile Gamma Camera," *Ann. Surg.*, vol. 253, no. 4, pp. 774–778, Apr. 2011.
- [9] D. Elson and G.-Z. Yang, "The Principles and Role of Medical Imaging in Surgery," in *Key Topics in Surgical Research and Methodology*, T. Athanasiou, H. Debas, and A. Darzi, Eds. Berlin, Heidelberg: Springer Berlin Heidelberg, 2010, pp. 529–543.
- [10] "Sentinel node biopsy What you can expect - Mayo Clinic." [Online]. Available: <http://www.mayoclinic.org/tests-procedures/sentinel-node-biopsy/basics/what-you-can-expect/prc-20013550>. [Accessed: 13-Jun-2016].
- [11] "Nuclear Medicine," *National Institute of Biomedical Imaging and Bioengineering*, 15-May-2013. [Online]. Available:

<https://www.nibib.nih.gov/science-education/science-topics/nuclear-medicine>. [Accessed: 14-Jun-2016].

[12] “Human Health Campus - Nuclear Medicine Handbook slides.” [Online].

Available: https://humanhealth.iaea.org/HHW/MedicalPhysics/e-learning/Nuclear_Medicine_Handbook_slides/index.html. [Accessed: 14-Jun-2016].

[13] T. E. Peterson and L. R. Furenlid, “SPECT detectors: the Anger Camera and beyond,” *Phys. Med. Biol.*, vol. 56, no. 17, pp. R145–R182, Sep. 2011.

[14] J. D. Mathews, A. V. Forsythe, Z. Brady, M. W. Butler, S. K. Goergen, G. B. Byrnes, G. G. Giles, A. B. Wallace, P. R. Anderson, T. A. Guiver, P. McGale, T. M. Cain, J. G. Dowty, A. C. Bickerstaffe, and S. C. Darby, “Cancer risk in 680 000 people exposed to computed tomography scans in childhood or adolescence: data linkage study of 11 million Australians,” *BMJ*, vol. 346, no. may21 1, pp. f2360–f2360, May 2013.

[15] “Computed Tomography (CT),” *National Institute of Biomedical Imaging and Bioengineering*, 15-May-2013. [Online]. Available: <https://www.nibib.nih.gov/science-education/science-topics/computed-tomography-ct>. [Accessed: 13-Jul-2016].

- [16] T. Wagner, J. Buscombe, G. Gnanasegaran, and S. Navalkissoor, "SPECT/CT in sentinel node imaging:," *Nucl. Med. Commun.*, vol. 34, no. 3, pp. 191–202, Mar. 2013.
- [17] R. A. Valdés Olmos, D. D. Rietbergen, S. Vidal-Sicart, G. Manca, F. Giammarile, and G. Mariani, "Contribution of SPECT/CT imaging to radioguided sentinel lymph node biopsy in breast cancer, melanoma, and other solid cancers: from 'open and see' to 'see and open,'" *Q. J. Nucl. Med. Mol. Imaging Off. Publ. Ital. Assoc. Nucl. Med. AIMN Int. Assoc. Radiopharmacol. IAR Sect. Soc. Radiopharm. Chem. Biol.*, vol. 58, no. 2, pp. 127–139, Jun. 2014.
- [18] "2.2 Basic Principles of MRI." [Online]. Available: <https://www.cs.sfu.ca/~stella/papers/blairthesis/main/node11.html>. [Accessed: 20-Jun-2016].
- [19] W. A. Kaiser, S. O. R. Pfeleiderer, and P. A. T. Baltzer, "MRI-guided interventions of the breast," *J. Magn. Reson. Imaging*, vol. 27, no. 2, pp. 347–355, Feb. 2008.
- [20] C. Li, S. Meng, X. Yang, D. Zhou, J. Wang, and J. Hu, "Sentinel lymph node detection using magnetic resonance lymphography with conventional

- gadolinium contrast agent in breast cancer: a preliminary clinical study,” *BMC Cancer*, vol. 15, Apr. 2015.
- [21] V. J. L. Kuijs, M. Moosdorff, R. J. Schipper, R. G. H. Beets-Tan, E. M. Heuts, K. B. M. I. Keymeulen, M. L. Smidt, and M. B. I. Lobbes, “The role of MRI in axillary lymph node imaging in breast cancer patients: a systematic review,” *Insights Imaging*, vol. 6, no. 2, pp. 203–215, Mar. 2015.
- [22] S. Oura, H. Tanino, T. Yoshimasu, T. Sakurai, Y. Kokawa, and Y. Okamura, “The usefulness of sentinel node biopsy with MRI-guided lymph node sampling in breast cancer,” *Nippon Rinsho Geka Gakkai Zasshi*, vol. 63, no. 7, pp. 1607–1611, 2002.
- [23] C. Chi, Y. Du, J. Ye, D. Kou, J. Qiu, J. Wang, J. Tian, and X. Chen, “Intraoperative Imaging-Guided Cancer Surgery: From Current Fluorescence Molecular Imaging Methods to Future Multi-Modality Imaging Technology,” *Theranostics*, vol. 4, no. 11, pp. 1072–1084, Aug. 2014.
- [24] G. Themelis, J. S. Yoo, K.-S. Soh, R. Schulz, and V. Ntziachristos, “Real-time intraoperative fluorescence imaging system using light-absorption correction,” *J. Biomed. Opt.*, vol. 14, no. 6, pp. 64012-64012–9, 2009.
- [25] O. Khullar, J. V. Frangioni, and Y. L. Colson, “Image-Guided Sentinel Lymph Node Mapping and Nanotechnology-Based Nodal Treatment in Lung

- Cancer using Invisible Near-Infrared Fluorescent Light,” *Semin. Thorac. Cardiovasc. Surg.*, vol. 21, no. 4, pp. 309–315, 2009.
- [26] S. L. Troyan, V. Kianzad, S. L. Gibbs-Strauss, S. Gioux, A. Matsui, R. Oketokoun, L. Ngo, A. Khamene, F. Azar, and J. V. Frangioni, “The FLARE™ Intraoperative Near-Infrared Fluorescence Imaging System: A First-in-Human Clinical Trial in Breast Cancer Sentinel Lymph Node Mapping,” *Ann. Surg. Oncol.*, vol. 16, no. 10, pp. 2943–2952, Oct. 2009.
- [27] Q. T. Nguyen and R. Y. Tsien, “Fluorescence-guided surgery with live molecular navigation — a new cutting edge,” *Nat. Rev. Cancer*, vol. 13, no. 9, pp. 653–662, Sep. 2013.
- [28] “Ultrasonography - MeSH - NCBI.” [Online]. Available: <http://www.ncbi.nlm.nih.gov/mesh/68014463>. [Accessed: 13-Jun-2016].
- [29] M. M. Nadrljanski, “Physical principles of ultrasound | Radiology Reference Article | Radiopaedia.org,” *Radiopaedia*. [Online]. Available: <http://radiopaedia.org/articles/physical-principles-of-ultrasound-1>. [Accessed: 13-Jun-2016].
- [30] J. Nori, E. Vanzi, M. Bazzocchi, F. N. Bufalini, V. Distanto, F. Branconi, and T. Susini, “Role of axillary ultrasound examination in the selection of breast

- cancer patients for sentinel node biopsy," *Am. J. Surg.*, vol. 193, no. 1, pp. 16–20, Jan. 2007.
- [31] A. R. Sever, P. Mills, S. E. Jones, K. Cox, J. Weeks, D. Fish, and P. A. Jones, "Preoperative Sentinel Node Identification With Ultrasound Using Microbubbles in Patients With Breast Cancer," *Am. J. Roentgenol.*, vol. 196, no. 2, pp. 251–256, Feb. 2011.
- [32] L. L. Montgomery, A. C. Thorne, K. J. Van Zee, J. Fey, A. S. Heerdt, M. Gemignani, E. Port, J. Petrek, H. S. Cody, and P. I. Borgen, "Isosulfan blue dye reactions during sentinel lymph node mapping for breast cancer," *Anesth. Analg.*, vol. 95, no. 2, p. 385–388, table of contents, Aug. 2002.
- [33] Boughey JC, Suman VJ, Mittendorf EA, and et al, "Sentinel lymph node surgery after neoadjuvant chemotherapy in patients with node-positive breast cancer: The acosog z1071 (alliance) clinical trial," *JAMA*, vol. 310, no. 14, pp. 1455–1461, Oct. 2013.
- [34] "Sentinel Lymph Node Surgery Not Appropriate for All Women Diagnosed With Breast Cancer," *Breastcancer.org*. [Online]. Available: <http://www.breastcancer.org/research-news/20131118:EF>. [Accessed: 13-Jul-2016].

- [35] S. Pesek, T. Ashikaga, L. E. Krag, and D. Krag, "The false-negative rate of sentinel node biopsy in patients with breast cancer: a meta-analysis," *World J. Surg.*, vol. 36, no. 9, pp. 2239–2251, Sep. 2012.
- [36] Y. Wang, H. Dong, H. Wu, L. Zhang, K. Yuan, H. Chen, M. Jiao, and R. Fu, "Improved false negative rate of axillary status using sentinel lymph node biopsy and ultrasound-suspicious lymph node sampling in patients with early breast cancer," *BMC Cancer*, vol. 15, p. 382, 2015.
- [37] K. J. Hachey and Y. L. Colson, "Current Innovations in Sentinel Lymph Node Mapping for the Staging and Treatment of Resectable Lung Cancer," *Semin. Thorac. Cardiovasc. Surg.*, vol. 26, no. 3, pp. 201–209, 2014.
- [38] K. Suga, Y. Yuan, M. Okada, N. Matsunaga, A. Tangoku, S. Yamamoto, and M. Oka, "Breast Sentinel Lymph Node Mapping at CT Lymphography with Iopamidol: Preliminary Experience," *Radiology*, vol. 230, no. 2, pp. 543–552, Feb. 2004.
- [39] Y. Liu, W. Akers, A. Q. Bauer, S. Mondal, K. Gullicksrud, G. Sudlow, J. P. Culver, and S. Achilefu, "Intraoperative Detection of Liver Tumors Aided by Fluorescence Goggle System and Multimodal Imaging," *The Analyst*, vol. 138, no. 8, pp. 2254–2257, Apr. 2013.

- [40] S. Keereweer, J. D. F. Kerrebijn, P. B. A. A. Driel, B. Xie, E. L. Kaijzel, T. J. A. Snoeks, I. Que, M. Hutteman, J. R. Vorst, J. S. D. Mieog, A. L. Vahrmeijer, C. J. H. Velde, R. J. B. de Jong, and C. W. G. M. Löwik, "Optical Image-guided Surgery—Where Do We Stand?," *Mol. Imaging Biol.*, vol. 13, no. 2, pp. 199–207, Jul. 2010.
- [41] F. Zhang, G. Niu, G. Lu, and X. Chen, "Preclinical Lymphatic Imaging," *Mol. Imaging Biol. MIB Off. Publ. Acad. Mol. Imaging*, vol. 13, no. 4, pp. 599–612, Aug. 2011.
- [42] A. Chatterjee, N. Serniak, and B. J. Czerniecki, "Sentinel Lymph Node Biopsy in Breast Cancer: A Work in Progress," *Cancer J. Sudbury Mass*, vol. 21, no. 1, pp. 7–10, 2015.
- [43] M. Tsuchimochi and K. Hayama, "Intraoperative gamma cameras for radioguided surgery: Technical characteristics, performance parameters, and clinical applications," *Phys. Med.*, vol. 29, no. 2, pp. 126–138, Mar. 2013.
- [44] F. Scopinaro, A. Tofani, G. di Santo, B. Di Pietro, A. Lombardi, M. Lo Russo, A. Soluri, R. Massari, C. Trotta, and C. Amanti, "High-Resolution, Hand-Held Camera for Sentinel-Node Detection," *Cancer Biother. Radiopharm.*, vol. 23, no. 1, pp. 43–52, Feb. 2008.

- [45] M. Tsuchimochi, H. Sakahara, K. Hayama, M. Funaki, R. Ohno, T. Shirahata, T. Orskaug, G. Maehlum, K. Yoshioka, and E. Nygard, "A prototype small CdTe gamma camera for radioguided surgery and other imaging applications," *Eur. J. Nucl. Med. Mol. Imaging*, vol. 30, no. 12, pp. 1605–1614, Sep. 2003.
- [46] J. N. Aarsvod, C. M. Greene, R. A. Mintzer, S. F. Grant, T. M. Styblo, N. P. Alazraki, B. E. Patt, G. M. Caravaglia, J. Li, and J. S. Iwanczyk, "Intraoperative gamma imaging of axillary sentinel lymph nodes in breast cancer patients," *Phys. Med.*, vol. 21, pp. 76–79, Jan. 2006.
- [47] C. Mathelin, S. Salvador, D. Huss, and J.-L. Guyonnet, "Precise Localization of Sentinel Lymph Nodes and Estimation of Their Depth Using a Prototype Intraoperative Mini γ -Camera in Patients with Breast Cancer," *J. Nucl. Med.*, vol. 48, no. 4, pp. 623–629, Apr. 2007.
- [48] H. Fujii, Y. Kitagawa, M. Kitajima, and A. Kubo, "Sentinel nodes of malignancies originating in the alimentary tract," *Ann. Nucl. Med.*, vol. 18, no. 1, pp. 1–12, Feb. 2004.
- [49] M. Tsuchimochi, K. Hayama, T. Oda, M. Togashi, and H. Sakahara, "Evaluation of the Efficacy of a Small CdTe γ -Camera for Sentinel Lymph Node Biopsy," *J. Nucl. Med.*, vol. 49, no. 6, pp. 956–962, Jun. 2008.

- [50] L. Vermeeren, R. A. V. Olmos, W. M. C. Klop, A. J. M. Balm, and M. W. M. van den Brekel, "A Portable γ -Camera for Intraoperative Detection of Sentinel Nodes in the Head and Neck Region," *J. Nucl. Med.*, vol. 51, no. 5, pp. 700–703, May 2010.
- [51] L. Vermeeren, R. A. V. Olmos, W. Meinhardt, and S. Horenblas, "Intraoperative Imaging for Sentinel Node Identification in Prostate Carcinoma: Its Use in Combination with Other Techniques," *J. Nucl. Med.*, vol. 52, no. 5, pp. 741–744, May 2011.
- [52] L. Vermeeren, W. Meinhardt, A. Bex, H. G. van der Poel, W. V. Vogel, C. A. Hoefnagel, S. Horenblas, and R. A. V. Olmos, "Paraortic Sentinel Lymph Nodes: Toward Optimal Detection and Intraoperative Localization Using SPECT/CT and Intraoperative Real-Time Imaging," *J. Nucl. Med.*, vol. 51, no. 3, pp. 376–382, Mar. 2010.
- [53] O. R. Brouwer, R. A. V. Olmos, L. Vermeeren, C. A. Hoefnagel, O. E. Nieweg, and S. Horenblas, "SPECT/CT and a Portable γ -Camera for Image-Guided Laparoscopic Sentinel Node Biopsy in Testicular Cancer," *J. Nucl. Med.*, vol. 52, no. 4, pp. 551–554, Apr. 2011.
- [54] P. Russo, A. S. Curion, G. Mettivier, M. Esposito, M. Aurilio, C. Caracò, L. Aloj, and S. Lastoria, "Evaluation of a CdTe semiconductor based compact

- gamma camera for sentinel lymph node imaging,” *Med. Phys.*, vol. 38, no. 3, pp. 1547–1560, Mar. 2011.
- [55] S. Vidal-Sicart, P. Paredes, G. Zanón, J. Pahisa, S. Martinez-Román, X. Caparrós, A. Vilalta, R. Rull, and F. Pons, “Added Value of Intraoperative Real-Time Imaging in Searches for Difficult-to-Locate Sentinel Nodes,” *J. Nucl. Med.*, vol. 51, no. 8, pp. 1219–1225, Aug. 2010.
- [56] P. Olcott, G. Pratx, D. Johnson, E. Mittra, R. Niederkohr, and C. S. Levin, “Clinical evaluation of a novel intraoperative handheld gamma camera for sentinel lymph node biopsy,” *Phys. Med.*, vol. 30, no. 3, pp. 340–345, May 2014.
- [57] K. Popovic, J. E. McKisson, B. Kross, S. Lee, J. McKisson, A. G. Weisenberger, J. Proffitt, A. Stolin, S. Majewski, and M. B. Williams, “Development and Characterization of a Round Hand-Held Silicon Photomultiplier Based Gamma Camera for Intraoperative Imaging,” *IEEE Trans. Nucl. Sci.*, vol. 61, no. 3, pp. 1084–1091, Jun. 2014.
- [58] IAEA, “Nuclear Medicine Physics,” 2015.
- [59] G. B. Saha, “Performance Parameters of Gamma Cameras,” in *Physics and Radiobiology of Nuclear Medicine*, Springer, 2013, pp. 127–151.

- [60] “NEMA Publishes NEMA NU 1-2012 Performance Measurements of Gamma Cameras - NEMA.” [Online]. Available: <https://www.nema.org/news/Pages/NEMA-Publishes-NEMA-NU-1-2012-Performance-Measurements-of-Gamma-Cameras.aspx>. [Accessed: 06-Jul-2016].
- [61] A. D. Murphy, A. Britten, and B. Powell, “Hot or not? The 10% rule in sentinel lymph node biopsy for malignant melanoma revisited,” *J. Plast. Reconstr. Aesthetic Surg. JPRAS*, vol. 67, no. 3, pp. 316–319, Mar. 2014.
- [62] R. Dutta, A. Klufftinger, M. MacLeod, G. Kindrachuk, and C. Baliski, “Revisiting the ‘10% rule’ in breast cancer sentinel lymph node biopsy: an approach to minimize the number of sentinel lymph nodes removed,” *Am. J. Surg.*, vol. 203, no. 5, pp. 623–627, May 2012.
- [63] V. T. D. M. D. Schatzlein, “Tutorial: Attenuation of X-Rays By Matter.” [Online]. Available: <http://www.spectroscopyonline.com/tutorial-attenuation-x-rays-matter>. [Accessed: 16-Jul-2016].
- [64] S. P. Povoski, J. O. Olsen, D. C. Young, J. Clarke, W. E. Burak, M. J. Walker, W. E. Carson, L. D. Yee, D. M. Agnese, R. V. Pozderac, N. C. Hall, and W. B. Farrar, “Prospective randomized clinical trial comparing intradermal, intraparenchymal, and subareolar injection routes for sentinel lymph node

- mapping and biopsy in breast cancer," *Ann. Surg. Oncol.*, vol. 13, no. 11, pp. 1412–1421, Nov. 2006.
- [65] K. Motomura, Y. Komoike, Y. Hasegawa, T. Kasugai, H. Inaji, S. Noguchi, and H. Koyama, "Intradermal radioisotope injection is superior to subdermal injection for the identification of the sentinel node in breast cancer patients," *J. Surg. Oncol.*, vol. 82, no. 2, pp. 91-96-97, Feb. 2003.
- [66] K. M. McMasters, S. L. Wong, R. C. Martin, C. Chao, T. M. Tuttle, R. D. Noyes, D. J. Carlson, A. L. Laidley, T. Q. McGlothlin, P. B. Ley, C. M. Brown, R. L. Glaser, R. E. Pennington, P. S. Turk, D. Simpson, P. B. Cerrito, M. J. Edwards, and University of Louisville Breast Cancer Study Group, "Dermal injection of radioactive colloid is superior to peritumoral injection for breast cancer sentinel lymph node biopsy: results of a multiinstitutional study," *Ann. Surg.*, vol. 233, no. 5, pp. 676–687, May 2001.
- [67] V. S. Klimberg, I. T. Rubio, R. Henry, C. Cowan, M. Colvert, and S. Korourian, "Subareolar Versus Peritumoral Injection for Location of the Sentinel Lymph Node," *Ann. Surg.*, vol. 229, no. 6, p. 860, Jun. 1999.